A&A 643, A141 (2020)
https://doi.org/10.1051/0004-6361/202038860

Astronomy & Astrophysics

Tracing the total molecular gas in galaxies: [CII] and the CO-dark gas*

S. C. Madden[1], D. Cormier[1], S. Hony[2], V. Lebouteiller[1], N. Abel[3], M. Galametz[1], I. De Looze[4,5], M. Chevance[6], F. L. Polles[7], M.-Y. Lee[8], F. Galliano[1], A. Lambert-Huyghe[1], D. Hu[1], and L. Ramambason[1]

[1] AIM, CEA, CNRS, Université Paris-Saclay, Université Paris Diderot, Sorbonne Paris Cité, 91191 Gif-sur-Yvette, France
e-mail: suzanne.madden@cea.fr
[2] Institut für Theoretische Astrophysik, Zentrum für Astronomie der Universität Heidelberg, Albert-Ueberle Str. 2, 69120 Heidelberg, Germany
[3] University of Cincinnati, Clermont College, 4200 Clermont College Drive, Batavia, OH 45103, USA
[4] Sterrenkundig Observatorium, Ghent University, Krijgslaan 281 S9, 9000 Gent, Belgium
[5] Department of Physics and Astronomy, University College London, Gower Street, London WC1E 6BT, UK
[6] Astronomisches Rechen-Institut, Zentrum für Astronomie der Universität Heidelberg, Mönchhofstrasse 12-14, 69120 Heidelberg, Germany
[7] LERMA, Observatoire de Paris, PSL Research University, CNRS, Sorbonne Université, 75014 Paris, France
[8] Korea Astronomy and Space Science Institute, 776 Daedeokdae-ro, 34055 Daejeon, Republic of Korea

Received 6 July 2020 / Accepted 14 August 2020

ABSTRACT

Context. Molecular gas is a necessary fuel for star formation. The CO (1−0) transition is often used to deduce the total molecular hydrogen but is challenging to detect in low-metallicity galaxies in spite of the star formation taking place. In contrast, the [C II]λ158 μm is relatively bright, highlighting a potentially important reservoir of H_2 that is not traced by CO (1−0) but is residing in the C^+-emitting regions.
Aims. Here we aim to explore a method to quantify the total H_2 mass (M_{H_2}) in galaxies and to decipher what parameters control the CO-dark reservoir.
Methods. We present Cloudy grids of density, radiation field, and metallicity in terms of observed quantities, such as [O I], [C I], CO (1−0), [C II], L_{TIR}, and the total M_{H_2}. We provide recipes based on these models to derive total M_{H_2} mass estimates from observations. We apply the models to the *Herschel* Dwarf Galaxy Survey, extracting the total M_{H_2} for each galaxy, and compare this to the H_2 determined from the observed CO (1−0) line. This allows us to quantify the reservoir of H_2 that is CO-dark and traced by the [C II]λ158 μm.
Results. We demonstrate that while the H_2 traced by CO (1−0) can be negligible, the [C II]λ158 μm can trace the total H_2. We find 70 to 100% of the total H_2 mass is not traced by CO (1−0) in the dwarf galaxies, but is well-traced by [C II]λ158 μm. The CO-dark gas mass fraction correlates with the observed $L_{[C II]}/L_{CO(1-0)}$ ratio. A conversion factor for [C II]λ158 μm to total H_2 and a new CO-to-total-M_{H_2} conversion factor as a function of metallicity are presented.
Conclusions. While low-metallicity galaxies may have a feeble molecular reservoir as surmised from CO observations, the presence of an important reservoir of molecular gas that is not detected by CO can exist. We suggest a general recipe to quantify the total mass of H_2 in galaxies, taking into account the CO and [C II] observations. Accounting for this CO-dark H_2 gas, we find that the star-forming dwarf galaxies now fall on the Schmidt–Kennicutt relation. Their star-forming efficiency is rather normal because the reservoir from which they form stars is now more massive when introducing the [C II] measures of the total H_2 compared to the small amount of H_2 in the CO-emitting region.

Key words. photon-dominated region – galaxies: ISM – galaxies: dwarf – HII regions – infrared: ISM

1. Introduction

Our usual view of star formation posits the molecular gas reservoir as a necessary ingredient, the most abundant molecule being H_2. This concept is borne out through testimonies of the first stages of star formation associated with and within molecular clouds and numerous observational studies showing the observed correlation of star formation with indirect tracers of H_2 reflected in the Schmidt–Kennicutt relationship (e.g. Kennicutt 1998; Kennicutt et al. 2007; Bigiel et al. 2008; Leroy et al. 2008, 2013; Genzel et al. 2012; Kennicutt & Evans 2012; Kumari et al. 2020). However, directly witnessing the emission of H_2 associated with the bulk of the molecular clouds is not feasible. Indeed, H_2 emits weakly in molecular clouds due to the lack of a permanent dipole moment and the high temperatures necessary to excite even the lowest rotational transitions (the two lowest transitions have upper level energies, $h\nu/k$, of 510 K and 1015 K). Therefore, H_2 observations can only directly trace a relatively small budget (15% to 30%) of warmer (~100 K) molecular gas in galaxies (e.g. Roussel et al. 2007; Togi & Smith 2016), but not the larger

* Data in Fig. 6 are only available at the CDS via anonymous ftp to cdsarc.u-strasbg.fr (130.79.128.5) or via http://cdsarc.u-strasbg.fr/viz-bin/cat/J/A+A/643/A141

reservoir of cold (~10−20 K) molecular gas normally associated with star formation.

In spite of four orders of magnitude lower abundance of CO compared to H_2, most studies rely on CO rotational transitions to quantify the properties of the H_2 reservoir in galaxies. The low excitation temperature of CO (1−0) (~5 K), along with its low critical density (n_{crit}) for collisional excitation (~10^3 cm^{-3}), make it a relatively strong, easily excited millimetre (mm) emission line to trace the cold gas in star-forming galaxies. Studies within our Galaxy long ago established a convenient recipe to convert the observed CO (1−0) emission line to H_2 gas mass, that is, the X_{CO} conversion factor (see Bolatto et al. 2013, for historical and theoretical development). Likewise, galaxies in our local universe have also routinely relied on CO observations to quantify the H_2 reservoir (e.g. Leroy et al. 2011; Bigiel et al. 2011; Schruba et al. 2012; Cormier et al. 2014, 2016; Saintonge et al. 2017). CO is also commonly used to probe the H_2 and star formation activity in the high-z ($z \sim 1-2$) universe (e.g. Tacconi et al. 2010, 2018, 2020; Daddi et al. 2010, 2015; Combes et al. 2013; Carilli & Walter 2013; Walter et al. 2014; Genzel et al. 2015; Kamenetzky et al. 2017; Pavesi et al. 2018), although for higher-z sources, higher J CO lines may become more readily available, but relating these to the bulk of the H_2 mass is less straightforward (e.g. Papadopoulos et al. 2008; Gallerani et al. 2014; Kamenetzky et al. 2018; Vallini et al. 2018; Dessauges-Zavadsky et al. 2020). Well-known caveats can hamper accurate total H_2 gas mass determination in galaxies based on observed CO emission only, including those associated with assumptions on CO excitation properties, dynamical effects related to X_{CO}, presence of ensembles of molecular clouds along the lines of sight in galaxies and low filling factor and abundance of CO compared to H_2, as in low-metallicity environments (e.g. Maloney & Black 1988; Glover & Mac Low 2011; Shetty et al. 2011; Narayanan et al. 2012; Pineda et al. 2014; Clark & Glover 2015; Bisbas et al. 2017).

However, CO can fail altogether to trace the full H_2 reservoir, particularly in low-metallicity galaxies. Lower dust abundance allows the far-ultraviolet (FUV) photons to permeate deeper into molecular clouds compared to more metal-rich clouds, photodissociating CO molecules, leaving a larger C^+-emitting envelope surrounding a small CO core. H_2, on the other hand, photodissociates via absorption of Lyman-Werner band photons, which, for moderate A_V, can become optically thick, allowing H_2 to become self-shielded from photodissociation (e.g. Gnedin & Draine 2014), leaving a potentially significant reservoir of H_2 existing outside of the CO-emitting core, within the C^+-emitting envelope (Fig. 1). The presence of this CO-dark molecular gas (e.g. Papadopoulos et al. 2002; Röllig et al. 2006; Wolfire et al. 2010; Glover & Clark 2012a) necessitates other means to trace this molecular gas reservoir that is not probed by CO. The total H_2 mass is therefore the CO-dark gas mass plus the H_2 within the CO-emitting core. Efficient star formation in this CO-dark gas has been shown theoretically to be possible (e.g. Krumholz & Gnedin 2011; Glover & Clark 2012b).

More recently, observations of the submillimetre (submm) transitions of [C I] have been used to trace the total H_2 gas mass in galaxies at high and low-z, especially due to the advent of the spectroscopic capabilities of SPIRE (Griffin et al. 2010) on the *Herschel* Space Observatory (Pilbratt et al. 2010) and with ALMA (Popping et al. 2017; Andreani et al. 2018; Jiao et al. 2019; Nesvadba et al. 2019; Bourne et al. 2019; Valentino et al. 2020; Dessauges-Zavadsky et al. 2020), while theory and simulations (Papadopoulos et al. 2004; Offner et al. 2014; Tomassetti et al. 2014; Glover & Clark 2016; Bothwell et al. 2017; Li et al. 2018; Heintz & Watson 2020) deem [C I] to be a viable tracer of CO-dark H_2. Likewise, ALMA has opened the window to numerous detections of [C II]λ158 μm in the high-z universe, making [C II], which is more luminous than [C I], a popular tracer of total H_2 in galaxies (e.g. Zanella et al. 2018; Bethermin et al. 2020; Schaerer et al. 2020; Tacconi et al. 2020). Dust mass estimates via monochromatic or full spectral energy distribution (SED) studies have also been used to quantify the total H_2 gas mass in the nearby and distant universe (e.g. da Cunha et al. 2013; Groves et al. 2015, more background on the different approaches to uncover CO-dark gas is presented in the following Sect. 2).

Local and global environmental effects, including star formation properties and metallicity, require consideration as well when choosing the approach to relate total gas mass to star formation. Low-metallicity environments present well-known issues in pinning down the molecular gas mass. Detecting CO in dwarf galaxies has been notoriously difficult (e.g. Leroy et al. 2009, 2012; Schruba et al. 2012; Cormier et al. 2014; Hunt et al. 2015; Grossi et al. 2016; Amorín et al. 2016, and references within), leaving us with uncertainties in quantifying the total molecular gas reservoir.

Star-forming dwarf galaxies often have super star clusters which have stellar surface densities greatly in excess of normal H II regions and OB associations. Thus, the dearth of detectable CO raises questions concerning the fueling of such active star formation. Possible explanations may include the following: (1) CO is not a reliable tracer of the total molecular gas reservoir; (2) there is a real under-abundance of molecular gas indicative of an excessively high star formation efficiency; (3) H_2 has been mostly consumed by star formation; (4) H_2 has been completely dissociated in the aftermath of star formation; and (5) HI is the important reservoir to host star formation.

These issues compound the difficulty in understanding the processes of both local and global star formation in low-metallicity environments. Developing reliable calibrators for the total M_{H_2} in low-metallicity galaxies is a necessary step to be able to refine recipes for converting gas into stars under early universe conditions and thus further our understanding of how galaxies evolve. Understanding the detailed physics and chemistry of the structure and properties of the gas that fuels star formation can help us to discriminate strategies for accurate methods to get to the bulk of the molecular gas in galaxies.

Since carbon is one of the most abundant species in galaxies, its predominantly molecular form, CO, and its neutral and ionised forms, C^0 and C^+, play important roles in the cooling of the interstellar medium (ISM) of galaxies. The locations of the transitions from ionised carbon, to neutral carbon, to CO, which are within the photodissociation region (PDR)-molecular cloud structure, depend on numerous local physical conditions, including the FUV radiation field strength (G_0)[1], hydrogen number density (n_H), gas abundances, metallicity (Z), dust properties, and so on. Low-metallicity star-forming environments seem to harbour unusual PDR properties compared to their dustier counterparts, with notably bright [C II]λ158 μm emission compared to the often faint CO (1−0) emission, characteristics that can be attributed to the lower dust abundance along with the star formation activity and clumpy ISM (e.g. Cormier et al. 2014; Chevance et al. 2016; Madden & Cormier 2019).

In this study, we determine a basic strategy to quantify the total H_2 mass in galaxies and estimate the CO-dark molecular

[1] 1 $G_0 = 1.6 \times 10^{-3}$ erg cm^{-2} s^{-1}, integrated over the energy range 6−13.6 eV (Habing 1968).

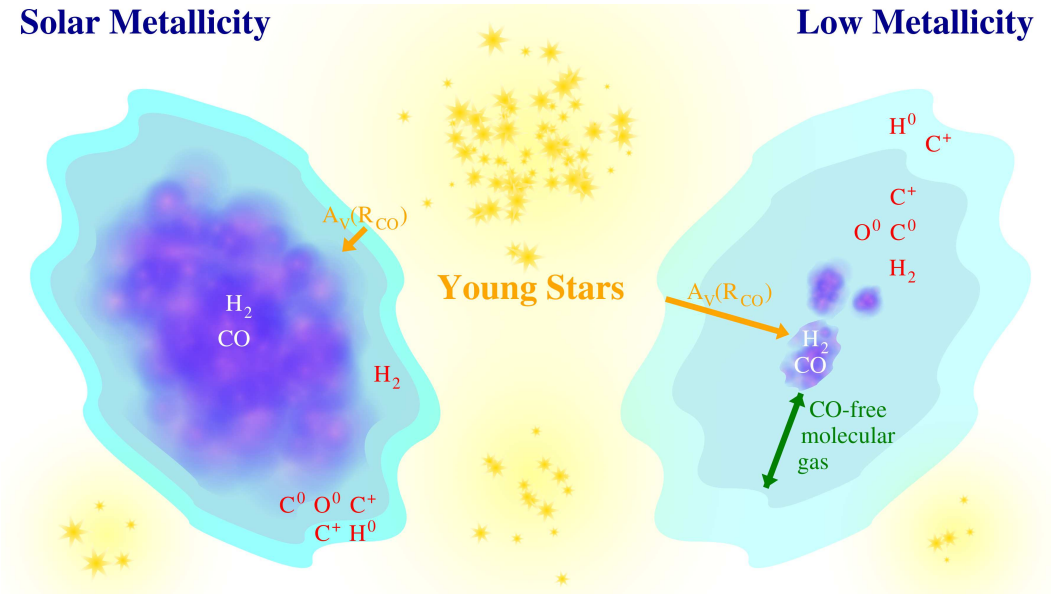

Fig. 1. Comparison of a solar metallicity (metal-rich) molecular cloud and a low-metallicity cloud impacted by the UV photons of nearby star clusters. The decrease in dust shielding in the case of the low-metallicity cloud leads to further photodissociation of the molecular gas, leaving a layer of self-shielded H_2 outside of the small CO-emitting cores. This CO-dark H_2 can, in principle, be traced by [C II] or [C I].

gas mass existing outside the CO-emitting core, for a range of Z, n_H, and G_0. We start with the models of Cormier et al. (2015, 2019), which were generated using the spectral synthesis code Cloudy (Ferland et al. 2017) to self-consistently model the mid-infrared (MIR) and far-infrared (FIR) fine structure cooling lines and the total infrared luminosity (L_{TIR}) from *Spitzer* and *Herschel*. This approach allows us to constrain the photoionisation and PDR region properties, quantifying the density and incident radiation field on the illuminated face of the PDR, G_0. These models exploit the fact that there is a physical continuity from the PDR envelope, where the molecular gas is predominantly CO-dark, into the CO-emitting molecular cloud. This dark gas reservoir can be primarily traced by the [C II]λ158 μm line while the $L_{[C\,II]}/L_{CO(1-0)}$ can constrain the depth of the molecular cloud and the $L_{[C\,II]}/L_{TIR}$ and $L_{[C\,II]}/L_{[O\,I]}$ constrain the G_0 and density at the illuminated face of the PDR (discussed in Sect. 5.2). With this study, we determine a conversion factor to pin down the total H_2, which will make use of the observed [C II], [O I], CO (1–0), and L_{TIR}. Application of the models to the star-forming low-metallicity galaxies of the *Herschel* Dwarf Galaxy Survey (DGS; Madden et al. 2013), using the observed [C II] and CO (1–0) observations, allows us to extract the total H_2 mass and determine the fraction of the total H_2 reservoir that is not traced by CO observations as a function of metallicity and other galactic parameters.

This paper is organised as follows. In Sect. 2 we review the studies that have focused on uncovering the CO-dark reservoir in galaxies. The environments of the dwarf galaxies in the DGS are briefly summarised in Sect. 3. In Sect. 4 we introduce the observational context and the motivations of this study by comparing the $L_{[C\,II]}/L_{CO(1-0)}$ and $L_{[C\,II]}/L_{FIR}$[2] of the full sample of the DGS to other more metal-rich galaxies from the literature. In Sect. 5 we present Cloudy model grids and discuss the effects of G_0, n_H, and metallicity. In this section we walk through the steps for using the models in order to understand the mass budget of the carbon-bearing species in the PDRs and to obtain the total H_2. In Sect. 6 we apply the models to the particular case of II Zw 40 observations, as an example. Section 7 discusses the model results applied to the DGS targets. In this section we extract the total H_2 for these galaxies and discuss the implication of the CO-dark gas reservoirs. We provide recipes to estimate the CO-dark H_2 and the total H_2 gas reservoir from [C II]. Possible caveats and limitations are noted in Sect. 8 and the results are summarised in Sect. 9.

2. CO dark gas studies

Three decades ago, the FIR spectroscopic window became readily accessible from the *Kuiper* Airborne Observatory (KAO) and the Infrared Space Observatory (ISO). First estimates of the CO-dark H_2 reservoir obtained from [C II]λ158 μm observations found that 10 to 100 times more H_2 was "hidden" in the C^+-emitting regions in dwarf galaxies compared to that inferred from CO (1–0) alone (Poglitsch et al. 1995; Madden et al. 1997). These early estimates, for lack of access to additional complementary FIR diagnostics to carry out detailed modeling, relied on a number of assumptions that have until now limited the use of the FIR lines to robustly quantify this CO-dark molecular gas in galaxies. Recent spatially resolved studies of [CII] in Local Group galaxies using *Herschel* and the Stratospheric Observatory for Infrared Astronomy (SOFIA) have also confirmed a significant presence of CO-dark gas (e.g. Fahrion et al. 2017; Requena-Torres et al. 2016; Jameson et al. 2018; Lebouteiller et al. 2019; Chevance et al. 2020). Additionally, the MIR rotational transitions of H_2 from *Spitzer* have been invoked to deduce a significant reservoir of H_2 in dwarf galaxies (Togi & Smith 2016). Other molecules observed in absorption, such as OH and HCO^+, have also been used as tracers of dark molecular gas in our Galaxy (Lucas & Liszt 1996; Allen et al. 2015; Xu et al. 2016; Li et al. 2018; Nguyen et al. 2018; Liszt et al. 2019). However, the need for sufficiently

[2] We note that for historical reasons, we use L_{FIR} when comparing observations of the DGS to other observations collected in the literature over the years, originally presented with L_{FIR}, such as Fig. 2, adapting L_{FIR} and L_{TIR} as per Rémy-Ruyer et al. (2013, 2015). However, this study uses L_{TIR} (3 to 1100 μm), which is more commonly used today.

high sensitivity and resolution limits their use in other galaxies.

As γ rays interact with hydrogen nuclei, they can trace the total interstellar gas. Comparison of γ ray observations in our Galaxy with CO and H^0 has uncovered an important reservoir of neutral dark gas that is not traced by CO or H I (Grenier et al. 2005; Ackermann et al. 2012; Hayashi et al. 2019). While γ ray emission, in principle, can be one of the most accurate methods possible to get at the total gas mass, its use to measure the total interstellar gas mass in other galaxies is limited for now because of the need for relatively high-resolution observations.

Comparison of *Herschel* [C II] velocity profiles to H I emission (Langer et al. 2010, 2014; Pineda et al. 2013; Tang et al. 2016) as well as observations comparing dust, CO (1−0), and H I (Planck Collaboration XIX 2011; Reach et al. 2017) confirm that this CO-dark gas reservoir can be an important component in our Galaxy, and comparable to that traced by CO (1−0) alone. Recent hydrodynamical simulations with radiative transfer and analytic theory also demonstrate the presence of this dark gas reservoir in the Galaxy that should be traceable via [C II] (Smith et al. 2014; Offner et al. 2014; Glover & Clark 2016; Nordon & Sternberg 2016; Gong et al. 2018; Franeck et al. 2018; Seifried et al. 2020) and is often associated with spiral arms in disc galaxies. While optically thick H I can, in principle, be the source of the CO-dark gas, there is no compelling evidence that it contributes significantly to the dark neutral gas (e.g. Murray et al. 2018). Therefore, we focus here on the CO-dark H_2 gas and the potential of C^+, in particular, to quantify the H_2 reservoir.

Dust mass measurements with *Planck*, compared to the gas mass measurements, have uncovered a reservoir of dark gas in the Galaxy (Planck Collaboration XIX 2011; Reach et al. 2015). Dust measurements have often provided easier means, in terms of observational strategy, to quantify the full reservoir of gas mass of galaxies in the local Universe as well as distant galaxies (e.g. Magdis et al. 2011; Leroy et al. 2011; Magnelli et al. 2012; Eales et al. 2012; Bourne et al. 2013; Sandstrom et al. 2013; Groves et al. 2015; Scoville et al. 2016; Liang et al. 2018; Bertemes et al. 2018). This approach also entails its own fundamental issues (e.g. Privon et al. 2018). The derived total molecular gas mass is a difference measure of two large quantities (H I-derived atomic gas mass and dust-derived total gas mass), which can result in large uncertainties. Dust mass determination, which is commonly derived via the modelling of the SED, requires constraints that include submm observations and necessitates dust models with assumed optical properties as a function of wavelength, composition and size distribution. Subsequently, turning total dust mass into total gas mass requires assumptions on dust-to-gas mass ratios which can carry large uncertainties depending on star formation history and metallicity and can vary by orders of magnitude, as shown by statistical studies of low-metallicity galaxies (e.g. Rémy-Ruyer et al. 2014; Roman-Duval et al. 2014; Galliano et al. 2018).

One contributing factor to the difficulty in being conclusive on the relationship of gas, dust, and star formation in low-metallicity conditions, in particular, is the fact that galaxies with full MIR to submm dust and gas modelling have been limited to mostly metal-rich environments and relatively higher star formation properties due to telescope sensitivity limitations. This impediment has been ameliorated with the broad wavelength coverage and the high spatial resolution and sensitivity of *Herschel*, allowing access to the gas and dust properties of low-metallicity galaxies. The DGS has compiled a large observational database of 48 low-metallicity galaxies (Madden et al. 2013), motivated by the *Herschel* PACS (Poglitsch et al. 2010) and *Herschel* SPIRE 55 to 500 μm photometry and spectroscopy capabilities.

3. Dwarf Galaxy Survey: extreme properties in low-metallicity environments

The DGS targeted the most important FIR diagnostic tracers, [C II]λ158 μm, [O I]λ63 μm, [O I]λ145 μm, [O III]λ88 μm, [N III]λ57 μm, [N II]λ122 μm, and [N II]λ205 μm (Cormier et al. 2012, 2015, 2019) in a wide range of low-Z galaxies, as low as $\sim$1/50 $Z_\odot$. Additionally, the DGS collected all of the FIR and submm photometry from *Herschel* to investigate the dust properties of star-forming dwarf galaxies. The IR SEDs exhibit distinct characteristics setting them apart from higher metallicity galaxies with different dust properties that generally exhibit overall warmer dust than normal-metallicity galaxies; for example their obvious paucity of PAH molecules and a striking non-linear drop in dust-to-gas mass ratios at lower metallicities ($Z < 0.1\,Z_\odot$; e.g. Galametz et al. 2011; Dale et al. 2012; Rémy-Ruyer et al. 2013, 2015).

[C II] usually ranks foremost amongst the PDR cooling lines in normal-metallicity galaxies, followed by the [O I]λ63 μm, with the $L_{[\mathrm{C\,II}]+[\mathrm{O\,I}]}/L_{\mathrm{FIR}}$ often used as a proxy of the heating efficiency of the photoelectric effect (e.g. Croxall et al. 2012; Lebouteiller et al. 2012, 2019). Cormier et al. (2015) summarised the observed FIR fine structure lines in the DGS noting that the range of $L_{[\mathrm{C\,II}]+[\mathrm{O\,I}]}/L_{\mathrm{FIR}}$ of low-metallicity galaxies is higher than that for galaxies in other surveys of mostly metal-rich galaxies (e.g. Brauher et al. 2008; Croxall et al. 2012; van der Laan et al. 2015; Cigan et al. 2016; Smith et al. 2017; Lapham et al. 2017; Díaz-Santos et al. 2017), indicating relatively high photoelectric heating efficiency in the neutral gas. However, in star-forming dwarf galaxies, the [O III]λ88 μm line is the brightest FIR line, not the [C II]λ158 μm line, as noted on full-galaxy scales (e.g. Cormier et al. 2015, 2019) as well as resolved scales (Chevance et al. 2016; Jameson et al. 2018; Polles et al. 2019). In more quiescent, metal-poor galaxies, however, the [C II]λ158 μm line is brighter than the [O III]λ88 μm line (e.g. Cigan et al. 2016). The predominance of the large-scale [O III]λ88 μm line emission, which requires an ionisation energy of 35 eV, demonstrates the ease at which such hard photons can traverse the ISM on full galaxy scales in star-forming dwarf galaxies (Cormier et al. 2010, 2012, 2015, 2019), highlighting the different nature and the porous structure of the ISM of low-metallicity galaxies. Since the [O III]/[C II] has been observed to also be similarly extreme in many high-z galaxies (e.g. Laporte et al. 2019; Hashimoto et al. 2019; Tamura et al. 2019; Harikane et al. 2020), the results presented here, where we focus on low-Z star-forming galaxies, may eventually be relevant to the understanding of the total molecular gas content and structure in some high-z galaxies.

4. $L_{[\mathrm{C\,II}]}/L_{\mathrm{CO(1-0)}}$ in galaxies

Figure 2 shows the CO (1−0) luminosity (L_{CO}) and [C II] luminosities ($L_{[\mathrm{C\,II}]}$) normalised by FIR luminosity (L_{FIR}) for a wide variety of environments, ranging from starburst galaxies and Galactic star forming regions to less active, more quiescent "normal" galaxies, low-metallicity star-forming dwarf galaxies, and some high-metallicity galaxies as well as some high-z galaxies. This figure, initially presented by Stacey et al. (1991) and subsequently used as a star-formation activity diagnostic, indicates that most normal and star forming galaxies are

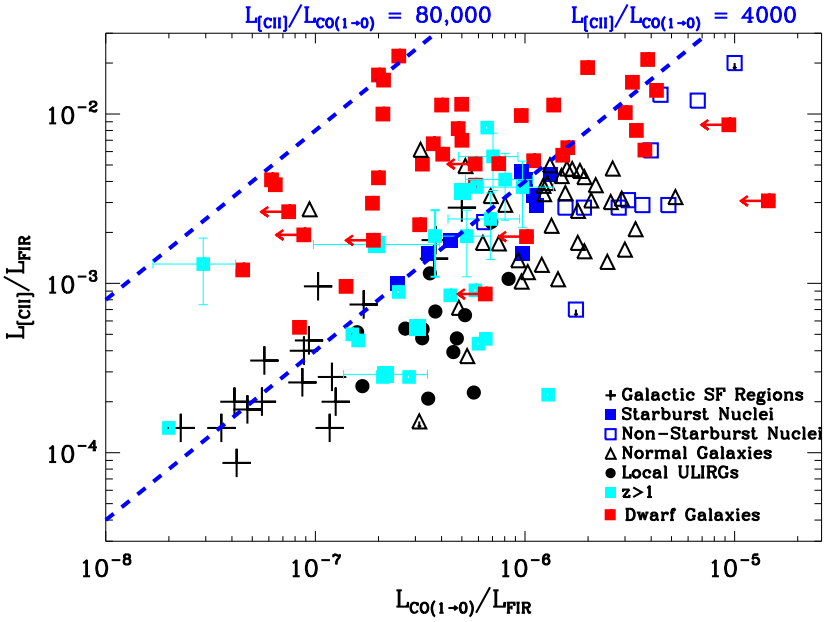

Fig. 2. $L_{CO(1-0)}/L_{FIR}$ vs. $L_{[C\,II]}/L_{FIR}$ observed in galaxies varying considerably in type, metallicity, and star formation properties. This is updated from Stacey et al. (1991, 2010), Madden (2000), and Hailey-Dunsheath et al. (2010) to include dwarf galaxies and more high-redshift galaxies. The dwarf galaxies are from Cormier et al. (2010, 2015) for the DGS; Grossi et al. (2016) for HeVICs dwarfs, and Smith & Madden (1997). High-redshift galaxies include those from Hailey-Dunsheath et al. (2010), Stacey et al. (2010), and Gullberg et al. (2015). The black and blue symbols are data from the original figure of Stacey et al. (1991) for Galactic star-forming regions, starburst nuclei and non-starburst nuclei, ULIRGS (Luhman et al. 2003), and normal galaxies (Malhotra et al. 2001). The dashed lines are lines of constant $L_{[C\,II]}/L_{CO(1-0)}$. We note the location of the low-metallicity dwarf galaxies (red squares) that show extreme observed $L_{[C\,II]}/L_{CO(1-0)}$ values.

observed to have $L_{[C\,II]}/L_{CO(1-0)} \sim 1000$ to 4000, with the more active starburst galaxies showing approximately a factor of three higher range of $L_{[C\,II]}/L_{CO(1-0)}$ than the more quiescent galaxies (Stacey et al. 1991, 2010; Hailey-Dunsheath et al. 2010). The more active dusty star forming environments possess widespread PDRs exposed to intense FUV and the $L_{[C\,II]}/L_{CO(1-0)}$ depends on the strength of the UV field and the shielding of the CO molecule against photodissociation due to H_2 and dust (e.g. Stacey et al. 1991, 2010; Wolfire et al. 2010; Accurso et al. 2017a).

It has already been shown that $L_{[C\,II]}$ is somewhat enhanced relative to L_{FIR} and more remarkably so relative to L_{CO} in a few cases of star-forming low-metallicity galaxies compared to more metal-rich galaxies (Stacey et al. 1991; Poglitsch et al. 1995; Israel et al. 1996; Madden et al. 1997, 2011; Hunter et al. 2001; Madden & Cormier 2019). In recent, larger studies, Cormier et al. (2015, 2019) carried out detailed modelling of the DGS galaxies and compared their overall physical properties to those of more metal-rich galaxies attributing the enhanced $L_{[C\,II]}/L_{FIR}$ to the synergy of their decreased dust abundance and active star formation. The consequence is a high ionisation parameter along with low densities resulting in a thick cloud and considerable geometric dilution of the UV radiation field. The effect over full galaxy scales is a low average ambient radiation field (G_0) and relatively normal PDR gas densities (often of the order of 10^3 to 10^4 cm^{-3}), with relatively large C^+ layers. This scenario is also coherent with the $L_{[C\,II]}/L_{CO(1-0)}$ observed in the low-metallicity galaxies.

As can be seen in Fig. 2, star-forming dwarf galaxies can reach $L_{[C\,II]}/L_{CO(1-0)}$ ratios an order of magnitude higher or more (sometimes reaching 80 000) than their more metal-rich counterparts on galaxy-wide scales. While CO (1−0) has been difficult to detect in star-forming low-metallicity galaxies, thus shifting these galaxies well off of the Schmidt–Kennicutt relation (e.g. Cormier et al. 2014), [C II], on the other hand, has been shown to be an excellent star formation tracer over a wide range of galactic environments, including the dwarf galaxies (e.g. de Looze et al. 2011, 2014; Herrera-Camus et al. 2015). Such relatively high [C II] luminosities in star-forming dwarf galaxies harbouring little CO (1−0) may be indicative of a reservoir of CO-dark gas, which is one of the motivations for this study.

5. Using a spectral synthesis code to characterise the ISM physical conditions

The strategy of this study is to first generate model grids that will help us explore how the properties of the CO-dark gas evolve as a function of local galaxy properties, such as Z, n_H, and G_0, and then to determine how observational parameters can be used to pin down the mass of the CO-dark gas. We show how $L_{[C\,II]}/L_{CO(1-0)}$ can constrain A_V from the models and then the $L_{[C\,II]}/L_{TIR}$ can narrow down the values of n_H and G_0 to finally quantify the total mass of H_2 and hence, the mass of H_2 that is not traced by CO, the CO-dark gas.

5.1. Model parameters and variations with cloud depth

We begin with the grids of Cormier et al. (2015, 2019), who use the spectral synthesis code Cloudy version 17.00 (Ferland et al. 2017), which simultaneously computes the chemical and thermal structure of H II regions physically adjacent to PDRs. The central source of the spherical geometry of the Cloudy model is the radiation extracted from Starburst99 (Leitherer et al. 2010) for a continuous starburst of 7 Myr and a total luminosity of $10^9\,L_\odot$. The grids were computed by varying the initial density at the illuminated face of the H II region, n_H, and the distance from the source to the edge of the illuminated H II region, the inner radius, r_{in}. The ionisation parameter (U) is deduced in the model based on the input ionising source, r_{in}, and n_H. The models are calculated for five metallicity bins: Z = 0.05, 0.1, 0.25, 0.5, and 1.0 $Z_\odot$[3], and n_H ranging from 10 to 10^4 cm^{-3}. The r_{in} values range from $\log(r_{in}\,\mathrm{cm}) = 20.0$ to 21.3 in steps of 0.3 dex, which for the various models covers a range of $U \sim 1$ to 10^{-5} and $G_0 \sim 17$ to 11481 in terms of the Habing radiation field.

A density profile that is roughly constant in the H II region and increases linearly with the total hydrogen column density (N_H) beyond 10^{21} cm^{-2} is assumed (Cormier et al. 2019). To ensure that all models go deep enough into the molecular phase, regardless of the metallicity, the stopping criterion of the models is set to a CO column density of $10^{17.8}$ cm^{-2} ($A_V \sim 10$ mag).

[3] We assume solar O/H = 4.9 × 10^{-4} (Asplund et al. 2009); i.e. $12 + \log(\mathrm{O/H})_\odot = 8.69$.

With this criterion, the optical depth of the CO(1−0) line, τ_{CO}, is greater than 1 in all models, which by our definition means that all models have transitioned in the molecular core[4]. For all calculations, the A_V/N_H ratio is computed self-consistently from the assumed grain-size distribution, grain types, and optical properties. For a more detailed description of the Cloudy models that generated the grids analysed here, see Appendix A.

Figure 3 shows the evolution of the accumulated mass, abundances, and intensities of the [C II], [C I], and CO (1−0) as a function of metallicity, density, temperature, and G_0 from the H^+ region into the molecular cloud. As we want to capture the properties of the H_2 zone, we have defined the location of the hydrogen ionisation front and the H_2 front in our calculations. As can be seen in the bottom subpanels in Fig. 3, the ionisation front is defined where H exists in the form of H^+ and H^0 with a ratio of 50/50; the transition between H^0 and H_2 is similarly where each species is 50% of the total hydrogen abundance. Our model results are relatively insensitive to the transition definitions. The C^+ zone is defined to be where 95% of the total carbon abundance is in the form of C^+ and 5% in the form of C^0 and likewise the C^0 zone has 95% of the total carbon abundance in the form of C^0 (Fig. 3 second and third subpanels).

To understand the effect of Z, n_H, and G_0 on the zone boundaries and accumulated mass, we compare three different cases in Fig. 3:

1. Metallicity effects: Compare $Z = 1.0\,Z_\odot$ (top left panel) and $Z = 0.1\,Z_\odot$ (top right panel) for a fixed n_H (10^3 cm^{-3}) and fixed G_0 (380).
2. Density effects: Compare $n_H = 10^2$ and 10^4 cm^{-3} with a fixed Z ($0.5\,Z_\odot$) and fixed G_0 (380) (middle left and right panels).
3. G_0 effects: Compare G_0 varying from 80 to 1800 with a fixed Z ($0.5\,Z_\odot$) and fixed n_H (10^3 cm^{-3}) (bottom left and right panels).

   Here we provide an example that can be used to interpret these plots: in the case of $Z = 1.0\,Z_\odot$ (top left panel), the transition from H^+ to H^0 occurs at $A_V \sim 0.015$ mag and the transition from H^0 to H_2 is at $A_V \sim 0.5$ mag, while the C^+-emitting zone spans the range of $A_V \sim 0.05$ to 2 mag. The evolution of the accumulated mass of the hydrogen species (top left panel, top subpanel) indicates that the C^+-emitting zone includes ∼90% of the total gas mass in the form of both H^0 and H_2, while CO is not yet formed at those A_V values. The C^0-emitting region begins at $A_V \sim 2$ mag until CO forms (in a region containing exclusively H_2). If we then lower the metallicity to $0.1\,Z_\odot$ (top right panel), we see that the evolution of the C^+-emitting zone and the H^0 and H_2 transitions in terms of A_V are the same as the $1.0\,Z_\odot$ case; however, the N_H, or cloud depth, scales differently, requiring a larger cloud depth at $0.1\,Z_\odot$ to reach the same A_V as the $1.0\,Z_\odot$ cloud.

The middle panels show how the cumulative [C II], [C I], and CO (1−0) intensities scale when changing only the n_H in the ionised zone from 10^2 cm^{-3} (middle left panel) to 10^4 cm^{-3} (middle right panel), while keeping G_0 and Z fixed. In this case, increasing the n_H shifts the transitions from H^+ to H^0 and from H^0 to H_2 to lower values of A_V. For the higher density case, we are quickly out of the H^+ region and into the atomic regime. Also, as can be seen from the central right-hand panel, C^+ is emitting over much of the H_2 zone and before CO is emitted for the higher density case.

Finally, the bottom panels demonstrate the effect of changing G_0 and keeping Z and n_H fixed. The increase of G_0 from 80 to 1800, for example, shifts the H^+ to H^0 transition to higher A_V values (from $A_V \sim 0.0015$ to 0.02 mag) as well as a higher N_H value for the H^0 to H_2 transition and with C^+ tracing a lower mass of H_2.

A_V/N_H is computed from the dust-to-gas ratio, which is assumed to be scaled by metallicity in the model for the range of metallicities studied here. For an H^+ region, as long as dust does not significantly compete with hydrogen for ionising photons, the N_H of the H^+ region will remain constant. However, reducing the metallicity does reduce the A_V corresponding to the N_H in the H^+ region by the same factor as the metallicity, and hence the ratio A_V/N_H. The size (in A_V) of the C^+ zone is roughly independent of metallicity (Kaufman et al. 2006), because the abundance of C^+ scales directly with metallicity, while the UV opacity scales inversely. For $Z = 0.1\,Z_\odot$ the carbon abundance is reduced by a factor of ten, but the decrease in dust extinction means that C^+ is formed over a path-length ten times longer than that for $1.0\,Z_\odot$.

5.2. Hydrogen and carbon phase transitions in the model grids

Another way to visualise the model grids is shown in Fig. 4 with some observables, such as H I, [C II], [C I], L_{TIR}, and [O I]λ63 μm. The y-axes of this figure show the $L_{[C\,II]}/L_{TIR}$ (in percentage) versus H I and H_2 gas mass reservoirs in the C^+ and C^0-emitting regions (defined above) extracted from Cloudy models for metallicities of $Z = 0.05$, 0.1, and $1.0\,Z_\odot$ (from top to bottom) and for a range of G_0 and n_H. The last column shows the $L_{[C\,II]}/L_{TIR}$ and $L_{[C\,II]}/L_{[O\,I]}$ behaviour in terms of G_0, n_H, and Z. The *total* H_2 gas mass from the model is shown in Col. 4 of Fig. 4 for the various metallicity bins. The C^+-emitting region and some of the C^0-emitting region, depending on Z, n, and G_0 (Fig. 3), will harbour H_2 sitting outside the CO-emitting region. We note that the models are scaled to L_{TIR} of 10^9 $L_\odot$. These diagrams can be used to bracket gas masses for a given $L_{[C\,II]}/L_{TIR}$ and Z bin. To apply these models to observations of a specific galaxy, the masses must be scaled by the proper L_{TIR} of the galaxy/10^9 $L_\odot$. More Cloudy model details, including application of the scaling factor, are described in Appendix A. An example of the application of the model grids to the galaxy IIZw 40 is demonstrated in Fig. 7 and Sect. 6. A simple conversion of observed [C II], [C I], or CO (1−0) to mass of total H_2 or fraction of CO-dark gas is not immediately straightforward.

5.2.1. Metallicity effects

As the metallicity decreases (from bottom to top panels in Fig. 4), the grids of gas mass shift to the right: more of the H_2 is associated with the C^+ and C^0-emitting zones, demonstrating the overall larger CO-dark gas reservoirs predicted by the models in order to reach the molecular core. The location of both the H_2 front and the formation of CO depend on metallicity, with both zones forming at higher A_V with decreasing Z (Wolfire et al. 2010). The location of the H_2 front as a function of A_V depends only weakly on metallicity, scaling as $\sim \ln(Z^{-0.75})$. This is caused by the H_2 formation rate scaling linearly with Z, while the UV dissociation rate of H_2 depends on both the self-shielding of H_2 (independent of Z) and dust extinction (which increases at a given depth with increasing Z). The CO-forming zone scales as $\sim \ln(Z^{-2})$ which is due to the decreased abundance of oxygen and carbon, which scale directly with Z. This has the overall

[4] To apply to specific cases where A_V is not necessarily ∼10 mag requires running the model to different cloud depths, as we discuss in Sect. 5.4, where we quantify the M_{H_2} of the individual DGS galaxies.

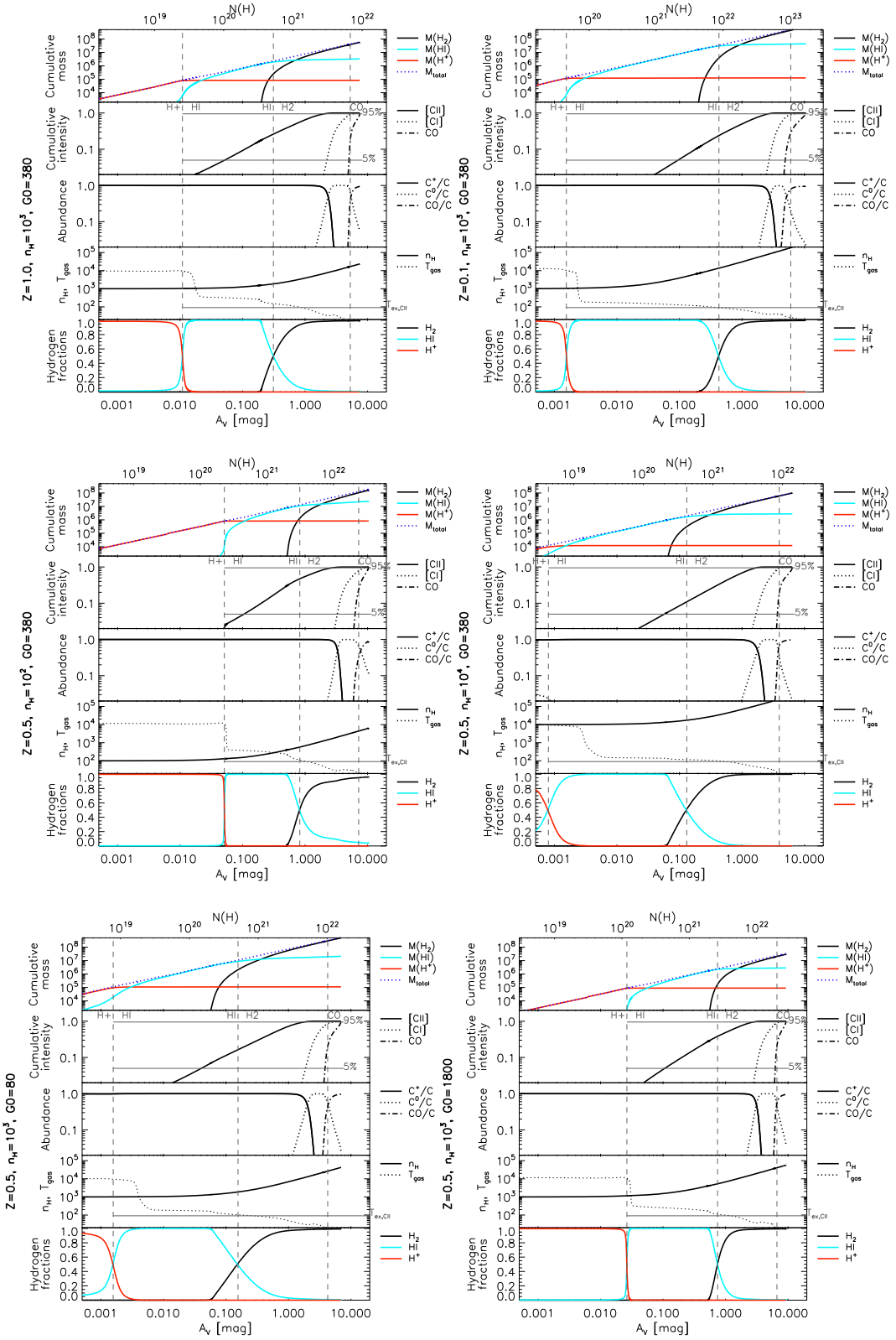

Fig. 3. Evolution of the modelled gas parameters, Z, $n_{\rm H}$, and $N_{\rm H}$, as a function of depth (A_V) for a solar-metallicity cloud (*top left*) and for a cloud of 0.1 $Z_\odot$ (*top right*), with a starting density of 10^3 cm^{-3} and $r_{\rm in}$ of $10^{20.7}$ cm, $G_0 = 380$ in terms of the Habing field. *Two central panels*: effect of density variations (*left*: $n_{\rm H} = 10^2$ cm^{-3}; *right*: $n_{\rm H} = 10^4$ cm^{-3}) for $Z = 0.5\,Z_\odot$ with $G_0 = 380$. *Bottom two panels*: effect of G_0 variations (*left*: $G_0 = 80$; *right*: $G_0 = 1800$) for constant Z (0.5 $Z_\odot$) and constant $n_{\rm H}$ (10^3 cm^{-3}). Each panel contains subpanels within, *from top to bottom*: cumulative mass in the ionised, neutral atomic, and molecular phases; normalised cumulative intensity of the [C II]λ158 μm, [C I]λ610 μm, and CO (1–0) lines; abundance of C^+, C^0, and CO relative to C; hydrogen density ($n_{\rm H}$) as a function of column density ($N_{\rm H}$) and A_V; fraction of hydrogen in the ionised, atomic, and molecular form. The vertical dashed lines indicate the depth of the main phase transitions: H^+ to H^0, H^0 to H_2, CO(1–0) optical depth of 1. Masses indicated here should be adjusted for individual galaxies, scaling as $L_{\rm TIR}$ (galaxy)/10^9 $L_\odot$, as the source luminosity of the model is 10^9 $L_\odot$ (see Appendix A).

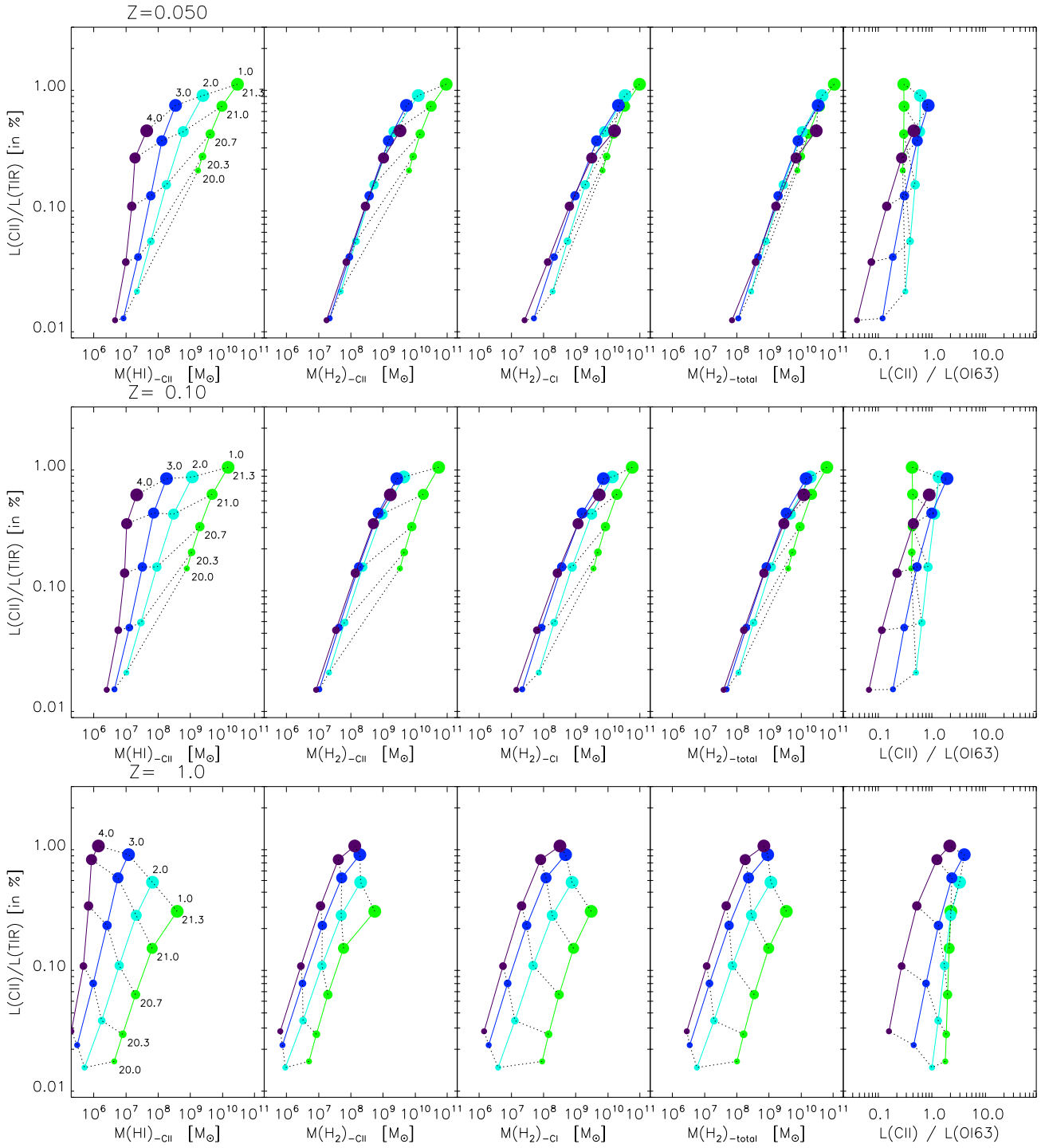

Fig. 4. Grids of Cloudy calculations: model $L_{[\mathrm{C\,II}]}/L_{\mathrm{TIR}}$ vs. H I and H_2 mass reservoirs in the C^+, C^0-emitting regions, total H_2 mass, and $L_{[\mathrm{C\,II}]}/L_{[\mathrm{O\,I}]}$ behaviour (last column) in terms of metallicities of $Z = 0.05$, 0.1, and $1.0\,Z_\odot$ (*from top to bottom*) and for a range of G_0 and n_{H}, the initial hydrogen density. The colour coding in each figure is log $n_{\mathrm{H}}/\mathrm{cm}^{-3}$ which increases from 1.0 (green) to 4.0 (purple). A range of G_0 is set by varying log r_{in}/cm from 21.3 at the top right of the grids (large dots) to 20.0 at the bottom left of the grids (smaller dots). These r_{in} values cover a range of log G_0 of 1.25 to 4.06 (Sect. 5). The Cloudy models are run with a source luminosity of $10^9\,L_\odot$. Thus, the output masses should be scaled likewise (see Appendix A for details). The models are run to log $N(\mathrm{CO})/\mathrm{cm}^{-2} = 17.8$ ($A_V \sim 10$ mag) for these grids.

effect of increasing the H_2 zone. Additionally, our calculations compute density as a function of column density. Decreasing Z increases the column density needed to obtain the same A_V (also in Fig. 3), therefore making the density in the H_2 zone higher at lower metallicity. These combined effects increase the mass present in the H_2 zone.

5.2.2. Distribution of the H^0 and H_2 phases

The first three columns of Fig. 4 show the consequence of metallicity on the partition of the mass between three regions, namely the H^0 associated with [C II] emission, the H_2 associated with [C II] emission, and the H_2 associated with [C I] emission. The

mass of H^0 associated with [C II] increases significantly with decreasing metallicity, as expected. The beginning of the H^0 zone starts at the hydrogen ionisation front, which for most of our parameter space is dominated by hydrogen opacity because the dust does not significantly compete with the gas for ionising photons. Therefore, the column density corresponding to the hydrogen ionisation front is nearly independent of Z, but the A_V of the ionisation front will decrease with decreasing Z because of the lower A_V/N_H. The A_V of the H_2 front increases slightly with decreasing Z as a result of decreased dust extinction. Overall, these two processes lead to a larger H^0 zone and, therefore, increased mass with decreasing Z. The size of the H_2 zone, and the beginning of the CO-emitting region, follow similar logic.

5.2.3. G_0 effects

When G_0 increases (for the same density and Z), the H_2 and CO fronts are pushed out to higher column densities, as expected because of the increased dissociation rate. The width (in A_V) of the H_2 zone therefore shows little variation with G_0. Increasing G_0 does have a mild effect on the mass associated with the H_2 zone, with increasing G_0 decreasing the mass in the H_2 zone (Fig. 4). This is because increasing G_0 moves the H_2 zone out to a larger column density (Fig. 3). As the density in our models increases with increasing N_H, the physical size of the H_2 zone will shrink. The thinner physical size leads to a smaller integrated mass when compared to a lower G_0 calculation. However, this effect is small when compared to variations of CO-dark mass with Z. Increasing density also slightly decreases the H_2 region mass, which is due to slight changes in the location of the H_2 front and the beginning of the CO formation zone.

5.2.4. Density effects

In addition to the size of each region, the temperature, n_H, and G_0 will dictate whether or not the H^0, H_2, and C^+ regions will emit, and therefore, trace the CO-dark gas. For [C II], the emission is controlled by the C^+ column density, the n_{crit} for [C II] emission (3×10^3 cm^{-3} for collisions with H^0), and the excitation temperature (92 K) (Kaufman et al. 1999). We see that a density below the n_{crit} in the H^0 region allows for efficient emission of [C II] (Fig. 3). This is reflected in the fact that, for the lower density models shown in Fig. 4, the H I mass and the H_2 mass traced by [C II] are often comparable. For densities beyond n_{crit}, the emission of [C II] is nearly independent of n_H, and is therefore controlled by the temperature and column density. Since the density increases with column density, for almost all models except the lowest density of 10 cm^{-3}, the density in the H_2 zone eventually exceeds n_{crit} of [C II], while for the H^0 zone the column density is lower, leading to lower densities in this region and a larger region of the parameter space with a density lower than n_{crit} of [C II]. This explains why Fig. 4 has some spread in the mass for different densities, while for the H_2, traced by [C II], the plot is nearly constant for decreasing Z, except for the lowest densities considered in our calculations. For $Z = 1.0\,Z_\odot$, slightly more spread is seen because the column density needed to reach the stopping criterion, and thus the density increase, is smaller. A similar effect occurs for the mass traced by [C I], which has a n_{crit} similar to [C II], thereby causing almost all of the lower metallicity calculations to be independent of n_H. Overall, the reservoir of M_{H_2} from which the C^+ emission originates, is systematically lower than that of the C^0-emitting zone. This effect is caused by the fact that where C^0 is emitting, most of the hydrogen is in the form of H_2 while in the C^+-emitting region, a significant amount of the hydrogen is in the form of H I, not necessarily in H_2, and the thickness of the respective layers are comparable.

The plots of the fifth column in Fig. 4 show the [C II]-to-[O I] ratio as a function of $L_{[C\,II]}/L_{TIR}$ for the range of n_H and G_0. Kaufman et al. (1999) show that this ratio depends strongly on G_0 for low density, especially for the higher Z case. Then, for increasing density the functional form of the ratio changes, becoming more sensitive to density for densities greater than the n_{crit} of [C II]. For larger densities, the [O I] emission increases with density, while the [C II] stays roughly constant (for a constant G_0), leading to a lower [C II] to [O I] ratio. This explains the trend of this plot with decreasing Z, as the increased density in the PDR, given our density law, leads to models with an initially low density reaching the n_{crit} of [C II], which causes the predicted emission of [O I] to increase relative to [C II].

Figure 4 allows us to quantify the amount of gas mass accumulated until the stopping criterion of the model is reached (i.e. log $N(CO) = 17.8$; refer to Sect. 5.1) as a function of important physical parameters, given the observed FIR spectrum. For example, in the metallicity bin $Z = 1.0\,Z_\odot$, given an observed $L_{[C\,II]}/L_{TIR}$ of 0.5%, the total mass of H_2 gas ranges from 1×10^8 to $3\times10^9\,M_\odot$, depending on the density, while for the lowest metallicity bin shown, $Z = 0.05\,Z_\odot$, the quantity of H_2 gas ranges from 1 to $3\times10^{10}\,M_\odot$ for this same $L_{[C\,II]}/L_{TIR}$ value. This shift to higher mass ranges of H_2 gas suggests that the mass of CO-dark H_2 gas can be an important component in low Z galaxies, as already pointed out in previous works (e.g. Papadopoulos et al. 2002; Wolfire et al. 2010).

In summary, from Fig. 4, the observed $L_{[C\,II]}/L_{TIR}$ enables us to determine a range of plausible G_0 and n_H for a given metallicity. If G_0 and n_H can be determined from other assumptions or observations (e.g. [C II]/[O I] for density) then a tighter constraint for the total H_2 gas can be determined (Sect. 5.4), eliminating some of the spread in n_H and G_0. For the lowest metallicity cases, the range of H_2, determined by G_0 and n_H, is relatively narrow, and less dependent on variations in G_0 or n_H. Thus, even having only observations of [C II] and L_{TIR}, Fig. 4 may bring a usefully narrow range of solutions for the total H_2 for the lowest metallicity cases based on the definition of CO-dark gas adopted here and used by Wolfire et al. (2010).

5.3. How [C II], [C I], and CO (1–0) can trace M_{H_2}

We extract the [C II], CO (1–0), and [C I](1–0) (609 μm) luminosities at the model stopping depth of log $N(CO) = 17.8$ ($A_V \sim 10$ mag), inspecting the line luminosities as a function of M_{H_2}. In Fig. 5 we show the $L_{[C\,II]}/M_{H_2}$, $L_{[C\,I]}/M_{H_2}$, and L_{CO}/M_{H_2} conversion factors as a function of n_H and G_0 for the examples of $Z = 1.0\,Z_\odot$ and $Z = 0.1\,Z_\odot$. Caution must be exercised when using L_{CO}/M_{H_2} from these figures, because the M_{H_2} within the CO-emitting region is very sensitive to the depth at which the models are stopped. If there is reason to trust that A_V of ~10 mag is an accurate representation of the CO-emitting zone, then the L_{CO}/M_{H_2} from this figure would be justifiable. It may not be applicable for some low Z cases, as discussed in Sect. 5.4.

We highlight the fact that the profiles shift to the right, to higher H_2 masses at lower Z. For the higher Z case, density in particular plays an important role in determining the M_{H_2} conversion factors for these species. For low Z, the density variations become less sensitive to the M_{H_2}, as noted in the $Z = 0.1\,Z_\odot$ case (right panel of Fig. 5). For the case of $L_{[C\,I]}/M_{H_2}$ and L_{CO}/M_{H_2} at lower metallicity, the density contours collapse together (Fig. 5, right panel), as is the case for the $L_{[C\,II]}$, except for the highest n_H case ($n_H = 10^4$ cm^{-3}; the green dots). In principle, [C I] should

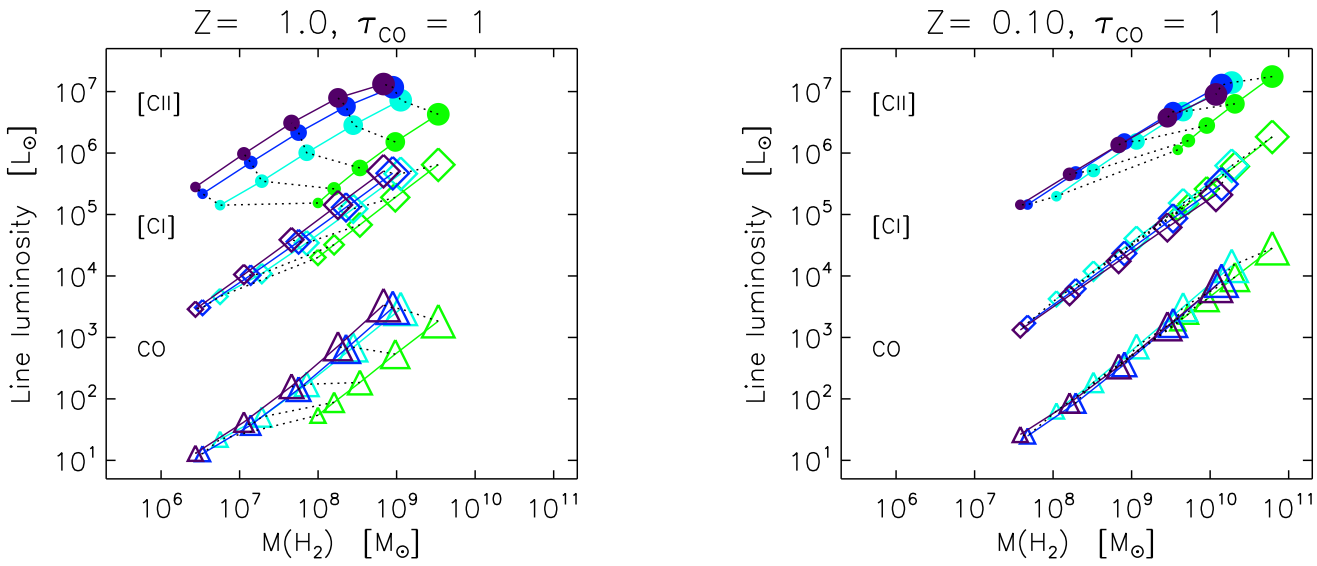

Fig. 5. Model grids that provide the $L_{[C\,II]}$, $L_{[C\,I]}(1-0)$ (609 μm), and L_{CO} – to – M_{H_2} conversion factors for $Z = 1.0\,Z_\odot$ (*left*) and $Z = 0.1\,Z_\odot$ (*right*) for the particular model using a cloud depth of log $N(CO)/cm^{-2} = 17.8$. The colour coding refers to density values ranging from log $n_H/cm^{-3} = 1$ (green) to 4 (purple). G_0 increases with increasing symbol size, taking values of 5, 20, 100, 200, and 500. To obtain the total molecular gas mass, which would include He, an additional factor of 1.36 (Asplund et al. 2009) should also be included for the total mass. We note that M_{H_2} in the CO-emitting region is very sensitive to the depth at which the models are stopped which corresponds to $A_V \sim 10$ mag here.

be able to quantify M_{H_2}, independent of density. From the right panel of Fig. 5, we derive a $L_{[C\,I]}/M_{H_2}$ conversion factor for the case of $Z = 0.1\,Z_\odot$:

$$M_{H_2} = 10^{4.06} \times {L_{[C\,I]}}^{1.04}, \quad (1)$$

where $L_{[C\,I]}$ is in units of $L_\odot$ and M_{H_2} is in units of $M_\odot$. Considering the small effects of density and G_0 on the $L_{[C\,I]}/M_{H_2}$ conversion factor for this particular low-Z case, Eq. (1) determines M_{H_2} from $L_{[C\,I]}$ with a standard deviation of 0.3 dex. The $L_{[C\,II]}/M_{H_2}$ is about two orders of magnitude higher than $L_{[C\,I]}/M_{H_2}$, while the L_{CO}/M_{H_2} is two orders of magnitude lower. [C I] appears to be a useful tracer to quantify the M_{H_2}, as also illustrated from hydrodynamical models (e.g. Glover & Clark 2016; Offner et al. 2014), and, as we show here at least for low-Z cases, with little dependence on n_H. The fact that $L_{[C\,I]}$ is much fainter than $L_{[C\,II]}$ (Fig. 5) makes it more difficult to use as a reliable tracer of M_{H_2}. These effects can also be seen from the grids in Fig. 4.

We continue in the following sections to demonstrate the use of the observed [C II] to determine M_{H_2} for specific cases and will follow up on [C I] as a tracer of M_{H_2} in a subsequent publication.

5.4. How to determine A_V and its effect on line emission (Spaghetti plots)

We see from Fig. 2 that $L_{[C\,II]}/L_{CO(1-0)}$ exhibits great variation from galaxy to galaxy. When comparing the observed $L_{[C\,II]}/L_{CO(1-0)}$ for low-metallicity galaxies (ranging from ~3000 to 80 000), to the modelled $L_{[C\,II]}/L_{CO(1-0)}$, where the stopping criterion is $A_V \sim 10$ mag, we see that the models do not reach such high observed $L_{[C\,II]}/L_{CO(1-0)}$ values. This is because when the models are stopped at $A_V \sim 10$ mag, too much CO has already formed for the low-Z cases (Fig. 3), which require the models to stop at lower A_V. The higher metallicity molecular clouds, exhibiting lower $L_{[C\,II]}/L_{CO(1-0)}$ than the dwarf galaxies, could be better described by stopping at $A_V \sim 10$ mag. To explore the sensitivity of the emission as a function of depth, we can use the observed $L_{[C\,II]}/L_{CO(1-0)}$ as a powerful constraint.

Figure 6 shows the model grid results for the $L_{[C\,II]}/L_{CO(1-0)}$ and ratios of [C II], CO (1−0), [C I]λ609 μm, [O I]λ63 μm, and [O I]λ145 μm lines to M_{H_2} as a function of A_V for a range of n_H ($10^1, 10^2, 10^3, 10^4\,cm^{-3}$) and G_0 values (~20, 500, 800) for $Z = 0.05\,Z_\odot$ (left column) and $Z = 1.0\,Z_\odot$ (right column). We can also understand the behaviour of these plots while referring to Fig. 3 and Sects. 5.1 and 5.2.

For example, when $A_V \sim 1$ mag is reached, [C II] formation is increasing rather linearly while CO increases exponentially (also evident in Fig. 3), and between $A_V \sim 1$ and 10 mag we see a rather linear decrease of $L_{[C\,II]}/L_{CO(1-0)}$. The $L_{[C\,II]}/M_{H_2}$ and $L_{[O\,I]}/M_{H_2}$ continue to decrease beyond $A_V \sim 1$ mag because the [C II] and [O I] have stopped emitting but the M_{H_2} continues to increase. The overall trend is therefore the drop in $L_{[C\,II]}/M_{H_2}$ and $L_{[O\,I]}/M_{H_2}$ for greater A_V. Density can have a considerable effect on the [O I] emission, producing a wide spread of $L_{[O\,I]}/M_{H_2}$ as A_V increases for higher G_0 environments. For example, for G_0 of 8000 and A_V ~5, there is about 50 to 100 times greater $L_{[O\,I]}/M_{H_2}$ for $n_H = 10^4\,cm^{-3}$ compared to the case with $n_H = 10^1\,cm^{-3}$ for $Z = 0.5$ and $1.0\,Z_\odot$. Both [O I] lines behave similarly, with [O I]λ145 μm being generally weaker than [O I]λ63 μm by approximately one order of magnitude.

The $L_{[C\,II]}/L_{CO(1-0)}$ is a good tracer of A_V for all G_0 and n_H, with the range of A_V becoming narrower for the spread of n_H as G_0 increases, as seen in the top panels of Fig. 6. The $L_{[C\,I]}/M_{H_2}$ begins to turn over, peaking at A_V of about a few magnitudes, approximately where the [C II] formation has decreased. This is why we see a relative flattening of the $L_{[C\,I]}/M_{H_2}$ for growing A_V.

We stop the plots in the figures beyond where CO has formed and becomes optically thick. Otherwise this M_{H_2} will continue to accumulate causing the L_{CO}/M_{H_2} to turn over and begin to decrease beyond the point of $\tau_{CO} = 1$. Having CO (1−0) observations in addition to the [C II] observations brings the best constraint on the A_V of the cloud and thus a better quantification of the M_{H_2}.

We note that to construct Fig. 6, the models are stopped at log $N(CO) = 17.8$ (a maximum $A_V \sim 10$ mag) and the line intensities are extracted at the different depths into the cloud, that is, at

different cloud A_V values. In principle, the emerging line intensities could be different depending on the stopping criterion, due to optical depth effects and cloud temperature structure. To quantified this effect, we ran grids stopping at several maximum A_V values (e.g. 2, 5, and 10 mag) and extracted line intensities, comparing the values we present in Fig. 6[5]. The effects on the [O I] and [C II] line intensities are mostly negligible (variations <20% throughout the grid). The intensities of the grid stopping at a maximum of A_V of 2 mag are generally similar to or larger than the line intensities extracted at the cloud depth of $A_V = 2$ mag of a grid stopping at maximum A_V of 10 mag, primarily due to optical depth effects on the grids run to A_V of 10 mag versus A_V of 2 mag. The CO (1−0) can see up to a factor of 2.5 variations (primarily at $A_V = 2$ mag) depending on the stopping criteria and the extraction of line intensities in A_V construction. Our comparison verification has assured us that we can move forward with our use of Fig. 6.

Later, when the models are applied to particular observations (Sect. 6), the depth of the models, that is, the maximum A_V, will be adapted for the specific metallicity case to determine the range of associated masses in the different zones. More precise determination of the stopping criterion will also require some knowledge of the range of G_0 and n_H (e.g. $L_{[C II]}/L_{[O I]}$ in Fig. 4). Only then can we have the necessary ingredients to obtain the total M_{H_2}. Thus, determination of A_V then gives us the total M_{H_2}.The mass of CO-dark H_2 is then the difference between the total M_{H_2} from the models and the H_2 determined from the observed CO (1−0) using a Galactic X_{CO}.

5.5. Quantification of the total M_{H_2} and CO-dark gas: how to use the models

We walk through the steps to constrain the total M_{H_2} and the CO-dark gas, depending on the availability of observations. We emphasise that to obtain the total molecular gas, including He, an additional factor of 1.36 (Asplund et al. 2009) should be taken into account. The best-constrained case is that for which [C II], [O I], CO (1−0), and L_{FIR} observations exist. We also illustrate the range of solutions that can be obtained with less observational constraints.

Since metallicity plays an important role in the models, knowledge or assumptions of Z are necessary. The parameters that define the applicable model are G_0, n_H, and the maximum A_V. We outline the steps to use the models:

– First we use the $L_{[C II]}/L_{FIR}$ to find the range of G_0 using Fig. 4. As can been seen in those figures the $L_{[C II]}/L_{FIR}$ is most strongly dependent on the radiation field density and less so on density for a given Z.

– The second step is to further refine the corresponding model parameters with the $L_{[C II]}/L_{[O I]}$ ratio (right-most panels in Fig. 4), or any combination of tracers that would provide the density in the [C II]-emitting zone of the PDR. For a given (range of) radiation field(s) this ratio is sensitive to the gas density. The combination of these two observational ratios generally constrains the radiation field and starting density well.

– Finally, the depth of the model (A_V) can be found using the observed $L_{[C II]}/L_{CO(1-0)}$ in combination with Fig. 6. The top series of panels shows the predicted line ratio for the different combinations of Z, G_0, and n_H.

[5] We provide the values of these plots in table form at the CDS where the reader can select model values of Z, n_H, inner radius (r_{in}), G_0, A_V, and τ_{CO} to obtain predicted M_{H_2}, [C II], CO (1−0), [C I], and [O I] luminosities.

These steps are illustrated for one galaxy, as an example, in Sect. 6 and Fig. 7.

Having found the parameter combination(s) that reproduce the relative strength of these key emission lines and the dust continuum, we can scale the model to the absolute line strength using the panels above and obtain the mass of H_2. Probably the most useful scaling is based on using the $L_{[C II]}/M_{H_2}$ predictions (fourth row of each panel in Fig. 6) because the [C II] line is strong and it originates throughout the parts of the model where the $L_{[C II]}/L_{CO(1-0)}$ varies strongly. We note that our methodology using [C I] as an observational constraint does not (directly) aid in better determining the most applicable models in the range of interest, that is, those situations where the CO-emitting zone is reached. However, the conversion from [C I] line luminosity to molecular gas mass for the applicable models is tighter than for [C II] (see also Fig. 5). Therefore [C I] observations will be very useful for getting the best possible measures of the total H_2 gas mass once the matching models have been determined and compared to observations. Once the total M_{H_2} is determined, the difference between this value and the M_{H_2} determined from CO (1−0) and the X_{CO} conversion factor will quantify the CO-dark gas reservoir.

6. Applying the models: the particular example of II Zw 40

Here, we use one galaxy from the DGS, II Zw 40, ($Z = 0.5\,Z_\odot$), to demonstrate how to determine the total M_{H_2} directly from the observations and the models presented above and thus the subsequent CO-dark gas mass. The relevant steps are visualised in Fig. 7, where the grids are run to a maximum depth of $A_V = 10$ mag. We first obtain the fiducial model results for M_{H_2} using the basic set of observational constraints: [C II], [O I], CO (1−0), and L_{FIR}. It is often not possible to have all of these tracers. Therefore, we also explore the derived ranges of M_{H_2} for II Zw 40 when limited observational data are available to constrain A_V, n_H, and G_0. In this way we can get an idea of what kind of accuracy can be obtained with varying availability of constraints.

6.1. Fiducial model

The observed value of $L_{[C II]}/L_{TIR}$ in II Zw 40 is 0.134 ± 0.024 (Cormier et al. 2015) which translates to a G_0 of around 300 for the range of densities considered. The $L_{[C II]}/L_{TIR}$ alone does not tightly constrain the density. In this case we also have the valuable [O I] line. The relatively high value of $L_{[C II]}/L_{[O I]}$ (1.35 ± 0.29) matches the lower density models ($\log(n_H) = 1.8$, from interpolation; last panel of Fig. 7a).

We retain the models that match the combined $L_{[C II]}/L_{TIR}$ and $L_{[C II]}/L_{[O I]}$, that is, the models that cross the yellow intersection in the right-most panel of Fig. 7a. Figure 7b, extracted from Fig. 6, shows the behaviour of $L_{[C II]}/L_{CO(1-0)}$ as a function of A_V for these models in grey. The green line is the model curve of the best matching model. As can be seen, all models reproduce the observed $L_{[C II]}/L_{CO(1-0)}$ (2.33×10^5) at an A_V value of ∼5 mag with a small dispersion.

Finally, the top panel of Fig. 7c shows that the $L_{[C II]}/M_{H_2}$ for the best matching model depth is ∼0.01 [$L_\odot/M_\odot$] but values up to ∼0.02 are also compatible. The $L_{[C II]}$ of $3.87 \times 10^6\,L_\odot$ of II Zw 40 translates to a total M_{H_2} ranging from $1.3–5.1 \times 10^8\,M_\odot$ with the best matching model yielding a M_{H_2} of $3.2 \times 10^8\,M_\odot$.

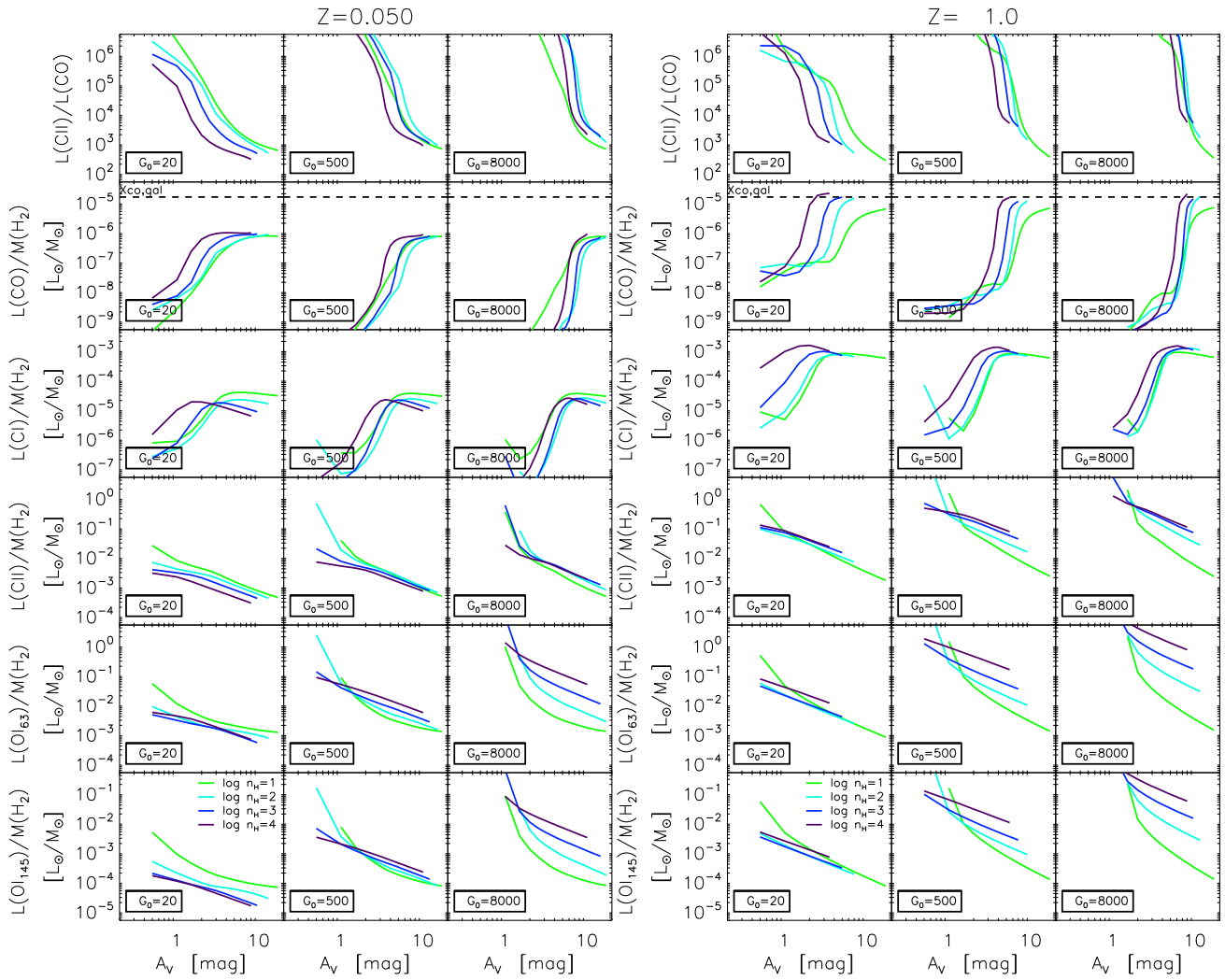

Fig. 6. "Spaghetti plots": model results for $L_{[\mathrm{C\,II}]}/L_{\mathrm{CO}(1-0)}$ and ratios of $L_{\mathrm{CO}}/M_{\mathrm{H_2}}$, $L_{[\mathrm{C\,I}]}\lambda609\,\mu\mathrm{m}/M_{\mathrm{H_2}}$, and $L_{[\mathrm{O\,I}]}/M_{\mathrm{H_2}}$ as a function of A_V for a range of n_{H} ($10^1, 10^2, 10^3, 10^4\,\mathrm{cm^{-3}}$) and G_0 values (~20, 500, 8000) for $Z = 0.05\,Z_\odot$ (*left*) and $1.0\,Z_\odot$ (*right*).

It is interesting to compare the derived H_2 gas mass with that determined using L_{CO} and a standard (Milky Way) X_{CO} conversion factor[6]. The standard conversion factor yields a value of $7.1 \times 10^6\,M_\odot$ which is only a few percent of the actual total H_2 gas mass determined from these models. We already know that as Z decreases, X_{CO} increases and calibrations for X_{CO} based on metallicity vary wildly in the literature (e.g. Bolatto et al. 2013). Thus, comparing with a Galactic X_{CO} really gives a lower limit on what is expected. In any case, even for the moderately low Z of $0.5\,Z_\odot$, the CO-dark molecular gas will be important.

6.2. Estimating M_{H_2} with fewer observational constraints

Following the full example for II Zw 40 above, we consider: case (a) when using [C II], CO (1–0), and L_{TIR} (no [O I] line observed or no other density indicator) and case (b) where only [C II] and L_{TIR} are available (CO (1–0) and [O I] are not available). In each case, we compare to the $M_{\mathrm{H_2}}$ derived from our fiducial model above (Sect. 6.1), where a more complete set of observations ([C II], L_{TIR}, [O I], and CO (1–0)) was available.

– case (a): Using [C II], L_{TIR}, and CO (1–0). The observed ratio of $L_{[\mathrm{C\,II}]}/L_{\mathrm{TIR}}$ for this galaxy (Fig. 7) indicates combinations of $\log(n_{\mathrm{H}})$ and $\log(G_0)$, from (1;2.2) through (2.5;2.8) to (4.0;3.3). For these models, A_V values between 3.5 and 6 mag reproduce $L_{[\mathrm{C\,II}]}/L_{\mathrm{CO}(1-0)}$ within its uncertainty. The best model, i.e. the closest predictions to the observed values, has an A_V of 4.5 mag and contains $1.3 \times 10^8\,M_\odot$ of H_2. The H_2 gas mass in the models that satisfactorily reproduces the observations ranges from 0.6 to $5.1 \times 10^8\,M_\odot$. Comparing with the range we find for the fiducial model ($1.3–5.1 \times 10^8\,M_\odot$), we can see that the allowed range is significantly larger: the upper value is the same, but now allows a lower end of the range. In the particular case of II Zw 40 the higher density models that contain less $M_{\mathrm{H_2}}$ gas before reaching the observed $L_{[\mathrm{C\,II}]}/L_{\mathrm{CO}(1-0)}$ values cannot be excluded and the range is therefore expanded to lower values.

– case (b): Using [C II] and L_{TIR} as the only available observational constraints; CO (1–0) has not been observed or with limited sensitivity and [O I] or another density tracer has not been observed. This means that we cannot exclude "normal" $L_{[\mathrm{C\,II}]}/L_{\mathrm{CO}(1-0)}$ ratios and high optical depth. Without a constraint on the A_V, these models can only be used to infer an upper limit on the $M_{\mathrm{H_2}}$ in the PDR by integrating the model until $\tau_{\mathrm{CO}} \simeq 1$.

[6] In this study, for the standard X_{CO} conversion we use a factor of $2 \times 10^{20}\,\mathrm{cm^{-2}(K\,km\,s^{-1})^{-1}}$ in terms of X_{CO} ($I_{\mathrm{CO}} \propto N_{\mathrm{H_2}}$); $3.2\,M_\odot\,\mathrm{pc^{-2}(K\,km\,s^{-1})^{-1}}$ in terms of α_{CO} ($I_{\mathrm{CO}} \propto M_{\mathrm{H_2}}$). While α_{CO} is normally $4.3\,M_\odot\,\mathrm{pc^{-2}(K\,km\,s^{-1})^{-1}}$, including helium, here we do not include the helium mass (factor of 1.36) when comparing to the model output of $M_{\mathrm{H_2}}$.

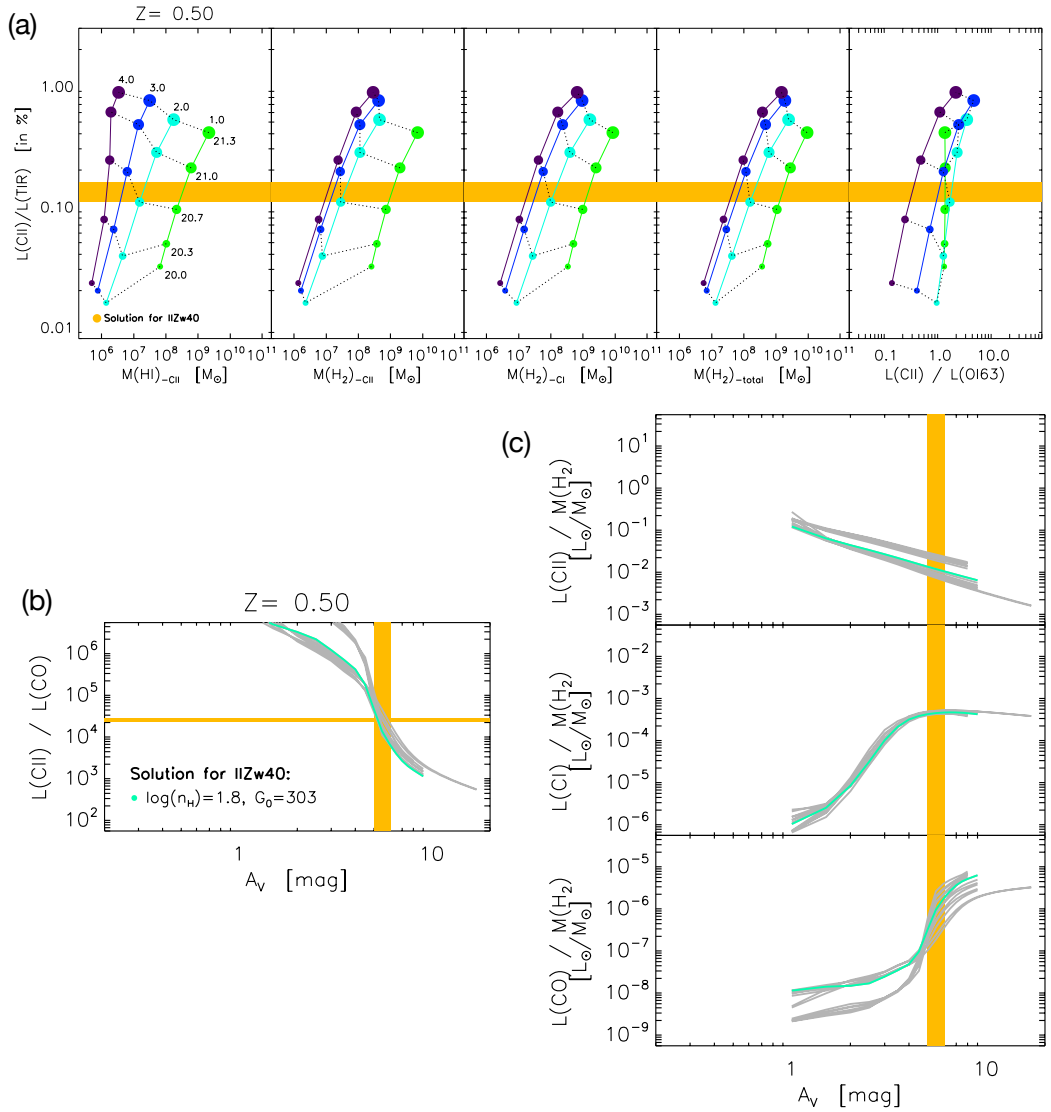

Fig. 7. Application of our model to the particular case of II Zw 40. *Panels a* show how the observed $L_{[\mathrm{C\,II}]}/L_{\mathrm{TIR}}$ and $L_{[\mathrm{C\,II}]}/L_{[\mathrm{O\,I}]}$ line ratios allow us to constrain n_{H} and G_0. *Panel b* shows how the $L_{[\mathrm{C\,II}]}/L_{\mathrm{CO}(1-0)}$ ratio evolves in II Zw 40 as a function of A_V, given the parameters previously derived from *panel a*. The green line indicates the best matching model. *Panels c* show the corresponding factors to convert $L_{[\mathrm{C\,II}]}$, $L_{[\mathrm{C\,I}]}$, and L_{CO} to $M_{\mathrm{H_2}}$ (see Sect. 6).

The same combinations of n_{H} and G_0 as for case *a* yield upper limits on H_2 gas masses of 0.7 to $13\times10^8\,M_\odot$. Removing the CO-bright H_2 gas from these models by using the predicted L_{CO} with a Galactic conversion factor yields upper limits on the dark H_2 gas mass of 0.5 to $11\times10^8\,M_\odot$. Thus the derived upper limit of $13\times10^8\,M_\odot$ is significantly above the value we derive ($3.2\pm1.9\times10^8\,M_\odot$) using the full set of constraints. Whether such an upper limit is useful will depend on the specific science question one is trying to address.

7. Quantification of the total $M_{\mathrm{H_2}}$ and CO-dark gas in the Dwarf Galaxy Survey

To quantify the CO-dark gas of the DGS galaxies, we determine the predicted total $M_{\mathrm{H_2}}$ for each DGS galaxy from the models ($M(\mathrm{H_2})_{\mathrm{total}}$). We then compare this predicted total $M_{\mathrm{H_2}}$ to the mass of the CO-bright H_2, $M(\mathrm{H_2})_{\mathrm{CO}}$, using the observed L_{CO} and Galactic X_{CO}. The mass of the CO-dark gas component, $M(\mathrm{H_2})_{\mathrm{dark}}$, would then be the difference between the model-predicted $M(\mathrm{H_2})_{\mathrm{total}}$ reservoir and the observed $M(\mathrm{H_2})_{\mathrm{CO}}$:

$$M(\mathrm{H_2})_{\mathrm{dark}} = M(\mathrm{H_2})_{\mathrm{total}} - M(\mathrm{H_2})_{\mathrm{CO}}. \quad (2)$$

We note n_{H} values in the range $10^{0.5}$–10^3 cm^{-3} and G_0 values of 10^2–10^3, which are determined from the Cormier et al. (2019) model solutions for the DGS galaxies, for metallicities ranging from near solar to $\approx1/50\,Z_\odot$[7]. We then extract the total $M_{\mathrm{H_2}}$ for each galaxy from the corresponding model grids, applying the steps described above, to quantify the total $M_{\mathrm{H_2}}$ consistent with the model solutions and consequently derive the CO-dark gas reservoir for each galaxy. Various galactic properties, observed and modelled parameters, and their relationships with the total H_2 mass and CO-dark gas reservoirs are inspected (Figs. 8–10).

[7] Metallicity values for the DGS galaxies are from Madden et al. (2013) which uses the strong line metallcity calibration from Pilyugin & Thuan (2005).

7.1. Trends of $M(H_2)_{total}$ and CO-dark gas with model parameters

We notice right away (Fig. 8) that for DGS galaxies, $M(\mathrm{H_2})_{\mathrm{total}}$ is always much larger than that determined using CO only, $M(\mathrm{H_2})_{\mathrm{CO}}$. The increasing $M(\mathrm{H_2})_{\mathrm{total}}/M(\mathrm{H_2})_{\mathrm{CO}}$ signals the effect of the CO-dark gas reservoir becoming an increasingly important component of the total $M_{\mathrm{H_2}}$, particularly in low-Z environments, which has been noted in the literature (e.g. Poglitsch et al. 1995; Israel et al. 1996; Madden et al. 1997; Wolfire et al. 2010; Fahrion et al. 2017; Nordon & Sternberg 2016; Accurso et al. 2017b; Jameson et al. 2018; Lebouteiller et al. 2019). The total mass of H_2 can range from 5 to a few hundred times the H_2 determined from the CO-emitting phase. The CO-dark gas dominates the total H_2 reservoir in these galaxies. We are clearly missing the bulk of the H_2 by observing only CO. What is controlling the fraction of CO-dark gas?

The G_0 and density determined from the models do not seem to play an obvious role in driving the CO-dark gas fraction as shown in Fig. 8 panels a and b. Panel c shows the tight anti-correlation of $M(\mathrm{H_2})_{\mathrm{total}}/M(\mathrm{H_2})_{\mathrm{CO}}$ with A_V, and, as shown in panel d, A_V anti-correlates with $L_{[\mathrm{C\,II}]}/L_{\mathrm{CO}(1-0)}$, underscoring the role of A_V in regulating the C^+ – CO phase transition in the PDR (e.g. Wolfire et al. 2010; Nordon & Sternberg 2016; Jameson et al. 2018). The extreme range of observed $L_{[\mathrm{C\,II}]}/L_{\mathrm{CO}(1-0)}$ in low-metallicity galaxies seen in Fig. 2 is a consequence of their overall low average effective A_V.

7.2. Trends of $M(H_2)_{total}$ and CO-dark gas with observables

What relationships exist between the observed quantities or measured galaxy properties and the total $M_{\mathrm{H_2}}$ and the quantity of CO-dark gas? In Fig. 9 (panel a) we see that the observed $L_{[\mathrm{C\,II}]}/L_{\mathrm{CO}(1-0)}$ is an excellent tracer of the CO-dark $M_{\mathrm{H_2}}$ fraction. We fit this correlation to convert from observed $L_{[\mathrm{C\,II}]}/L_{\mathrm{CO}(1-0)}$ to the $M(\mathrm{H_2})_{\mathrm{total}}/M(\mathrm{H_2})_{\mathrm{CO}}$:

$$M(\mathrm{H_2})_{\mathrm{total}}/M(\mathrm{H_2})_{\mathrm{CO}} = 10^{-3.14} \times [L_{[\mathrm{C\,II}]}/L_{\mathrm{CO}(1-0)}]^{1.09}. \quad (3)$$

The standard deviation of this fit is 0.25 dex. It follows from Eqs. (2) and (3) that the ratio of the mass of CO-dark gas to CO-bright gas is therefore:

$$M(\mathrm{H_2})_{\mathrm{dark}}/M(\mathrm{H_2})_{\mathrm{CO}} = 10^{-3.14} \times [L_{[\mathrm{C\,II}]}/L_{\mathrm{CO}(1-0)}]^{1.09} - 1.0. \quad (4)$$

We find a very tight correlation between $L_{[\mathrm{C\,II}]}$ and total H_2 gas mass (Fig. 9, panel b). The observed $L_{[\mathrm{C\,II}]}$ can thus convert directly to *total* $M_{\mathrm{H_2}}$:

$$M(\mathrm{H_2})_{\mathrm{total}} = 10^{2.12} \times [L_{[\mathrm{C\,II}]}]^{0.97}, \quad (5)$$

with a standard deviation of 0.14 dex. The C^+ luminosity alone can pin down the total $M_{\mathrm{H_2}}$, making the [C II]λ158 μm a valuable tracer to quantify the molecular gas mass in galaxies. Our modelling results find about a factor of three greater mass of total H_2 associated with $L_{[\mathrm{C\,II}]}$, and hence a larger reservoir of CO-dark gas mass, than that determined empirically from Zanella et al. (2018). These latter authors determine the $M_{\mathrm{H_2}}$ from an assumed CO-to-$M_{\mathrm{H_2}}$ conversion factor which is lower then that found in this study. We find a trend of the CO-dark $M_{\mathrm{H_2}}$ fraction growing as the metallicity decreases (Fig. 9, panel c).

Our study of the lowest metallicity objects, however, is limited by the lack of robust CO detections in these extreme environments, thus limiting our knowledge of the behaviour of Z with the CO-dark gas mass or total $M_{\mathrm{H_2}}$ at the lowest Z end. The CO-dark gas mass fraction does climb steeply as the Z decreases, even for moderately low-Z galaxies.

We see a weak trend of increasing fraction of CO-dark gas mass as the observed $L_{[\mathrm{C\,II}]}/L_{\mathrm{TIR}}$ increases (Fig. 9, panel d). For the relatively narrow range of $L_{[\mathrm{C\,II}]}/L_{\mathrm{TIR}}$ there is a wide range of CO-dark gas fraction. The fraction of CO-dark gas, which covers almost two orders of magnitude, does not show a trend with the approximately one order of magnitude range of surface density of SFR (Σ_{SFR}) in our galaxy sample (Fig. 9, panel e). This is consistent with the effect of increasing $L_{[\mathrm{C\,II}]}/L_{\mathrm{TIR}}$ (larger fraction of CO dark gas) being correlated with the increasing $L_{[\mathrm{C\,II}]}$ (Fig. 9, panel d) and less so with direct effects of L_{TIR}.

7.3. Consequences of the CO-dark gas fraction on the Schmidt–Kennicutt relation and the X_{CO} conversion factor

What is the consequence of the presence of this reservoir of CO-dark H_2 on Σ_{SFR} and the surface density of gas (Σ_{gas}) in galaxies, as described in the relationships of Kennicutt (1998) and Bigiel et al. (2008)? In panel a of Fig. 10, we determine the $\Sigma_{\mathrm{M_{H_2}}}$ within the CO-emitting region (black squares) and find their positions to be well off of the $\Sigma_{\mathrm{M_{H_2}}}$–$\Sigma_{\mathrm{SFR}}$ relationships, as found by Cormier et al. (2014), which may be suggestive of much higher Σ_{SFR} for their $M_{\mathrm{H_2}}$. Once we take into account the total $M_{\mathrm{H_2}}$ determined from [C II] and the modelling, which now includes the CO-dark $M_{\mathrm{H_2}}$ as well as the CO-bright $M_{\mathrm{H_2}}$ (Fig. 10, panel a; red dots), we see the locations of the galaxies shift to the right, lying between both $\Sigma_{\mathrm{M_{H_2}}}$–$\Sigma_{\mathrm{SFR}}$ relationships. The CO-dark gas is an important component to take into account in understanding the star formation activity in dwarf galaxies. While the data are limited, we find that taking into account the *total* $M_{\mathrm{H_2}}$, the star-forming dwarf galaxies do show a similar relation to that shown by the star-forming disc galaxies. Therefore, they are not necessarily more efficient in forming stars.

It has been shown from simulations (e.g. Glover & Clark 2012a; Krumholz et al. 2011) that star formation can proceed without a CO prerequisite, as well as without H_2. The relationship observed between H_2 and star formation can be due to the cloud conditions providing the ability to shield themselves from the UV radiation field, thereby allowing them to cool and form stars. In this process of shielding, at least H_2 formation can also proceed, as well as CO in well-shielded environments. The conditions required to reach the necessary low gas temperatures set the stage for efficient C^+ cooling. CO may accompany star formation but does not have a causality effect. Thus it may not come as a surprise to see star-forming dwarf galaxies that harbour a dearth of CO showing a similar relationship as that of the more metal-rich disc galaxies seen in the Schmidt–Kennicutt relationship.

With our determination of total H_2 we can now give an analytic expression to convert from observed CO to a total $M_{\mathrm{H_2}}$ conversion factor, α_{CO}, and its relationship with Z. Here, again, the total $M_{\mathrm{H_2}}$ now includes the CO-dark gas plus the CO-bright H_2 mass. We find from Fig. 10 (panel b):

$$\alpha_{\mathrm{CO}} = 10^{0.58} \times [Z/Z_{\odot}]^{-3.39}, \quad (6)$$

with a standard deviation of 0.32 dex. We find a steeply rising α_{CO} as the metallicity decreases. For example, at $Z = 0.2\,Z_{\odot}$, α_{CO} is about two orders of magnitude greater than that for the Galaxy. A strong dependence of the CO-to-H_2 conversion factor on metallicity is not unexpected. As the survival of molecules depends on how unsuccessful UV photons are in penetrating

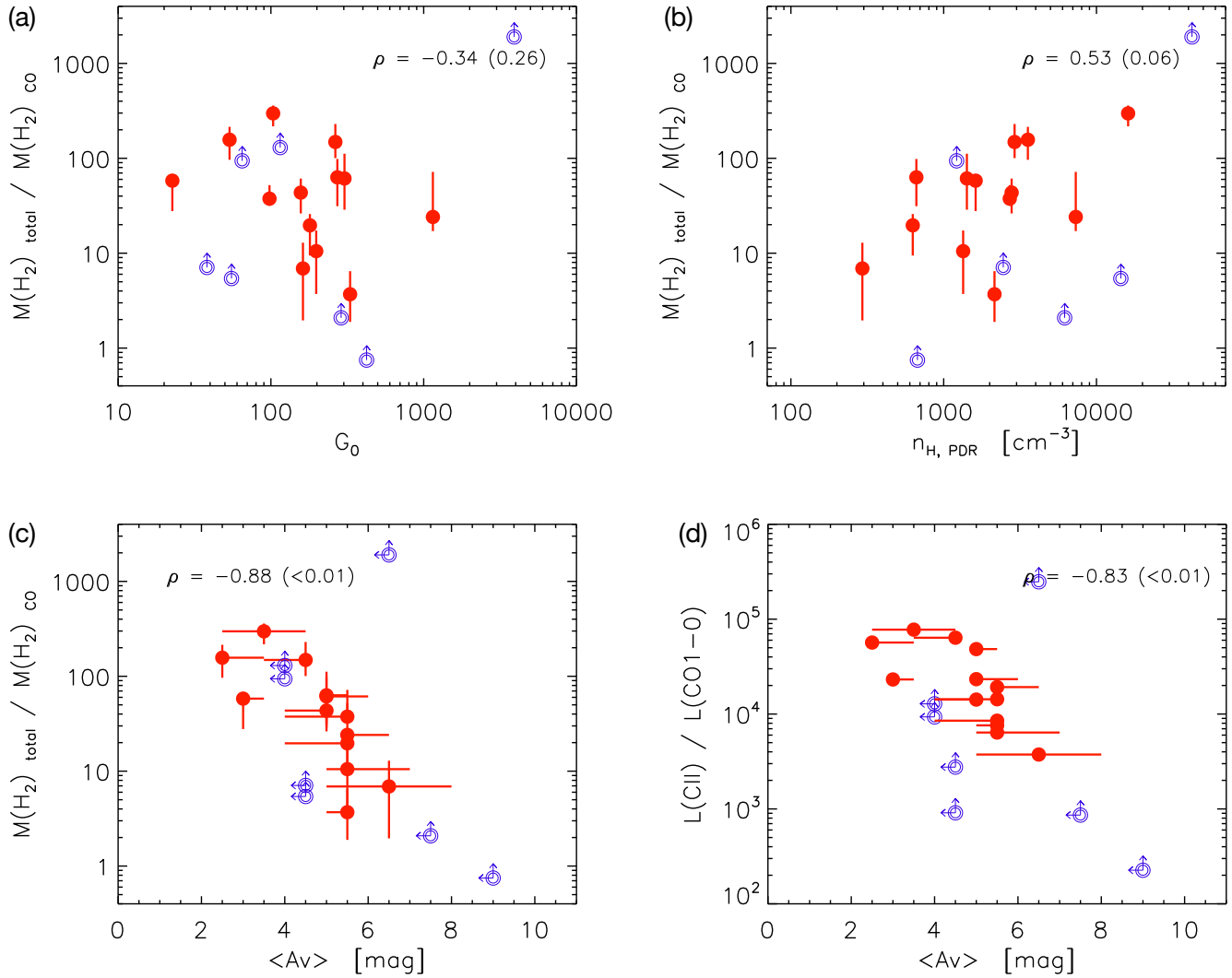

Fig. 8. Results from applying the models to the DGS sample and trends with model parameters. The vertical axis in *panels a–c* is $M(\mathrm{H_2})_{\mathrm{total}}/M(\mathrm{H_2})_{\mathrm{CO}}$ (the ratio of the total $M_{\mathrm{H_2}}$ determined from the model and the CO-bright $M_{\mathrm{H_2}}$ determined from CO observations and the Galactic conversion factor) versus, on the horizontal axis, (*a*) G_0, (*b*) density, and (*c*) A_V. *d*: observed $L_{[\mathrm{C\,II}]}/L_{\mathrm{CO(1-0)}}$ vs. model A_V. Spearman correlation coefficients (ρ) and p-values in parenthesis are indicated within each panel. Red points are solutions for the DGS galaxies with CO detections. Open symbols are upper limits due to CO non-detections. The masses determined by the model for the individual galaxies have been scaled by their proper L_{TIR}.

molecular clouds and photodissociating the molecules, extinction plays an important role in this process. Therefore, the lower dust abundance comes into play in the low-metallicity cases. In panel b of Fig. 10 we show a comparison of our derived metallicity dependence of α_{CO} with others in the literature. Schruba et al. (2012) determined α_{CO} from the observed SFR scaled by the observed L_{CO} and a constant depletion time. This approach assumes that the efficiency of conversion of H_2 into stars is constant within different environments. Our determination of α_{CO} is relatively comparable to that of Schruba et al. (2012)[8] given the spread of the observations, low number statistics, as well as possible uncertainties in metallicity calibrations. The α_{CO} from our study seems to climb even more steeply toward lower Z. However, the lower end of the metallicity space, where mostly only upper limits in CO (1−0) observations exist, is not pinned down robustly. It is well shifted up from the Glover & Mac Low (2011) relationship with CO-to-$M_{\mathrm{H_2}}$ conversion factor, which is determined from hydrodynamical simulations. A shallower slope is found for star-forming low-metallicity galaxies from Amorín et al. (2016) who derive a metallicity-dependent α_{CO} considering the empirical correlations of SFR, CO depletion timescale, and metallicity. Other $\alpha_{\mathrm{CO}}-Z$ scaling functions, such as those of Arimoto et al. (1996) and Wolfire et al. (2010), fall near that of Amorín et al. (2016).

By studying how the molecular gas depletion times vary with redshift and their relation to the star-forming main sequence, Genzel et al. (2015) determined a scaling of α_{CO} taking into account CO and dust-based observations (Fig. 10, panel b). While this conversion factor is shallower than the one we find from our study of local low-Z dwarf galaxies, these latter authors note that their study, which is based on massive star-forming galaxies, is probably not reliable for $Z < 0.5\,Z_{\odot}$. Accurso et al. (2017b) determine a comparable scaling of α_{CO} with Z to that of Genzel et al. (2015) using similar surveys, but include a second-order dependence on distance from the star-forming main sequence in their α_{CO}. Accurso et al. (2017b)

[8] While different relations have been shown for different categories of galaxies in Schruba et al. (2012), here we use the relation given for all of the galaxies in that study.

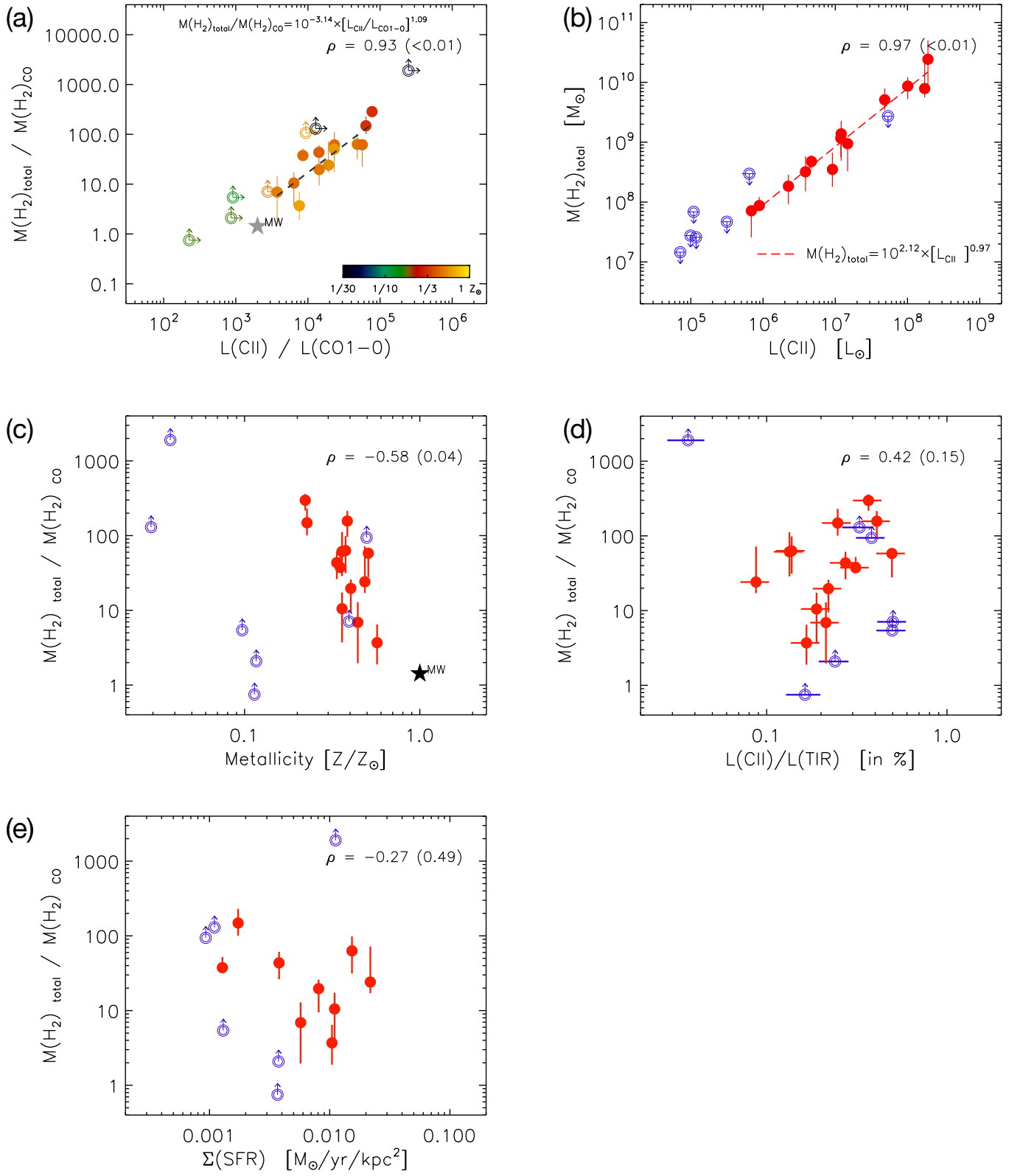

Fig. 9. Results for the DGS sample and trends with observable parameters. The vertical axis of *panels a, c, d,* and *e* is $M(H_2)_{total}/M(H_2)_{CO}$ (total M_{H_2} determined from the model over the M_{H_2} determined from CO observations and the Galactic conversion factor). The horizontal axes of these same panels are as follows: *a*: $L_{[C\,II]}/L_{CO(1-0)}$ with colour code for Z. The correlation shown in the dashed line is described in the panel in the equation for $M(H_2)_{total}/M(H_2)_{CO}$ as a function of the observed $L_{[C\,II]}/L_{CO(1-0)}$; standard deviation is 0.25 dex. *b*: total M_{H_2} determined from the models vs. the observed $L_{[C\,II]}$. Our resulting relationship of M_{H_2} as a function of $L_{[C\,II]}$ is given within the panel; standard deviation is 0.14 dex. *c*: $M(H_2)_{total}/M(H_2)_{CO}$ vs. Z; *d*: $M(H_2)_{total}/M(H_2)_{CO}$ vs. observed $L_{[C\,II]}/L_{TIR}$. *e*: $M(H_2)_{total}/M(H_2)_{CO}$ vs. Σ_{SFR}, where SFR is determined from total IR luminosity from Rémy-Ruyer et al. (2015). Spearman correlation coefficients (ρ) and p-values in parenthesis are indicated within each panel. Red points are DGS galaxies with CO detections. Open symbols in all panels are upper limits due to CO non-detections.

caution against using this relation below $Z \sim 0.1\,Z_\odot$, where it has not been calibrated. Bolatto et al. (2013) take a thorough look at numerous observations and theory and different metallicity regimes and propose a Z-dependent α_{CO} which is similar to that of Genzel et al. (2015) for near-solar Z galaxies, but curves to steeper α_{CO} for lower Z cases, while Tacconi et al. (2018) propose a compromise between those of Bolatto et al. (2013) and Genzel et al. (2015); see Fig. 10, panel b.

As soon as the ISM of the galaxy is more metal-poor, given the observed CO, which even for moderately metal-poor galaxies is difficult to obtain, the conversion factor from CO-to-H_2 quickly grows. Even at 20% $Z_\odot$, the CO conversion factor is already 1000 times that of our Galaxy. The true reservoir of M_{H_2} may have been severely underestimated so far at low Z and these new relations can quantify that.

8. Possible caveats and limitations

While [C II] emission can be a convenient tool to quantify a reservoir of molecular gas that is not traced by CO (1–0), there are some caveats and limitations to this study.

– Lower metallicity bound: We emphasise that the relationships used to determine total gas mass presented here have only been studied for the star-forming dwarf galaxies of the DGS with metallicities as low as $\approx 1/50\,Z_\odot$. The models have been applied for the low-metallicity galaxies for which CO is observed and this has limited the derived α_{CO} and $L_{[C\,II]}$-to-M_{H_2} conversion factor only to metallicities as low as $Z \sim 0.2\,Z_\odot$, even though [C II] has been detected in DGS galaxies below this metallicity.

– Limited range of model parameters: The models have been applied over a range of $n_H = 10$ to 10^4 cm^{-3} and over a range of inner radii corresponding to log $G_0 \sim 1$ to 4. These results need to be studied over broader ranges of galactic properties to be applied with confidence beyond this study. For example, faint, low-metallicity, more quiescent dwarf galaxies can also harbour star formation rates lower than those found for the Schmidt–Kennicutt relation (e.g. Roychowdhury et al. 2009; Cigan et al. 2016), in contrast to the DGS sample (Fig. 10, panel a). Some of these more quiescent dwarf galaxies are at the lowest metallicity range explored here and do not have CO detections, but may also be harbouring some CO-dark molecular gas. Likewise, more massive, CO-rich galaxies have yet to be tested with this model.

– Galactic size scales: These conclusions have been drawn on unresolved galaxy scales. The reliability of [C II] to trace M_{H_2} on resolved scales using these models has not been tested. A similar approach was carried out at 10 pc resolution in the 30Doradus region of the low-metallicity LMC ($Z = 0.5\,Z_\odot$), where >75% of the H_2 was CO-dark and traced by [C II] (Chevance et al. 2020). Considering that the [C II] emission is expected to be more extended than the CO (1–0) (e.g. Jameson et al. 2018; Chevance et al. 2020), our simple scheme using Cloudy and representing galaxies with a single H II region + molecular cloud in one dimension does not account for realistic geometry and for the physical mixing of different physical components and thus mixing G_0 and n_H conditions.

– The origin of [C II] emission in galaxies: We note that [C II] can arise from other components in galaxies, not only from neutral PDRs. For example [C II] can originate in the low-density ionised gas component in galaxies that is excited by electrons. In principle, to use [C II] to quantify the M_{H_2}, it is necessary to first determine whether or not there is "contamination" of the [C II] emission arising from the ionised gas which should first be removed before application of the model. This requires observations of other ionised gas tracers, such as the commonly used FIR [N II] lines, for example. Such studies often conclude that most of the [C II] emission in galaxies arises from PDR regions, with a decreasing fraction of the total [C II] emission arising from the ionised gas with decreasing metallicity (Kaufman et al. 2006; Croxall et al. 2017; Jameson et al. 2018; Cormier et al. 2019; Herrera-Camus et al. 2016; Accurso et al. 2017a; Sutter et al. 2019). Also, in our study we have not taken into account any contributing molecular gas reservoirs originating in the WNM or CNM atomic phases. The atomic gas component in our Galaxy has been proposed to harbour almost 50% of dark molecular gas of M_{H_2} (e.g. Kalberla et al. 2020). We do extract the H I mass from the models, but with the observations of our global studies we cannot yet explore this component. Most of the H I in the dwarf galaxies arises throughout the galaxies and often from a very extended component – extending well beyond the [C II] emission. We do not resolve the H I associated with the PDRs and therefore cannot address this point.

– Metallicity calibrations: A word of caution related to metallicity determination is necessary when applying these scaling relations. Metallicity calibrations are well known to differ (e.g. Kewley & Ellison 2008) and where absolute calibrations differ significantly, this should be taken into account when looking into detailed application of the models.

While this study points to the usefulness of [C II] as a tracer of the molecular gas in low-Z galaxies, enlarging the galactic parameter space will be needed to apply these findings in a more general sense to a wide variety of galaxies, especially galaxies more massive than the dwarf galaxies in this study. Here, we only focus on galaxies of the local universe. However, this is already a potential step forward in the possibility of estimating the gas mass from high-z galaxies using ALMA to access the [C II]$\lambda 158\,\mu$m in the cases where CO (1–0) may be faint, perhaps due to lower metallicity.

9. Summary and conclusions

This study is motivated by the extreme $L_{[C\,II]}/L_{CO(1-0)}$ values observed for low-metallicity galaxies, almost reaching 10^5 on global scales, which can be up to an order of magnitude higher than dustier star-forming galaxies. The bright [C II]$\lambda 158\,\mu$m lines observed in low-metallicity galaxies have been challenging to reconcile with the faint or undetectable CO (1–0) in light of their star formation activity. We have investigated the effects of metallicity, gas density, and radiation field on the total molecular gas reservoir in galaxies and quantified the mass of H_2 not traced by CO (1–0), that is, the CO-dark molecular gas that can be traced by [C II]. We inspected Cloudy grids traversing these physical parameters in order to understand the behaviour of observed quantities, such as [O I], [C I], CO (1–0), [C II], and L_{FIR} in terms of M_{H_2} as a function of A_V, metallicity and n_H. In principle, [C I] can be an important tracer of the CO-dark molecular gas, and this will be further investigated in a follow-up study. However, due to its higher luminosity, [C II] is an ideal tracer of the molecular gas. We give recipes on how to use these models to go from observations to total M_{H_2}. We apply the models to the *Herschel* DGS, extracting the total M_{H_2} for each galaxy. The CO-dark M_{H_2} is then determined from the difference between the total M_{H_2} and the CO-bright H_2 traced by the observed CO (1–0). Our findings indicate that CO (1–0) in the dwarf galaxies traces only a small fraction of the H_2, if any, while the total M_{H_2} is dominated by the CO-dark gas which can be uncovered by [C II] observations.

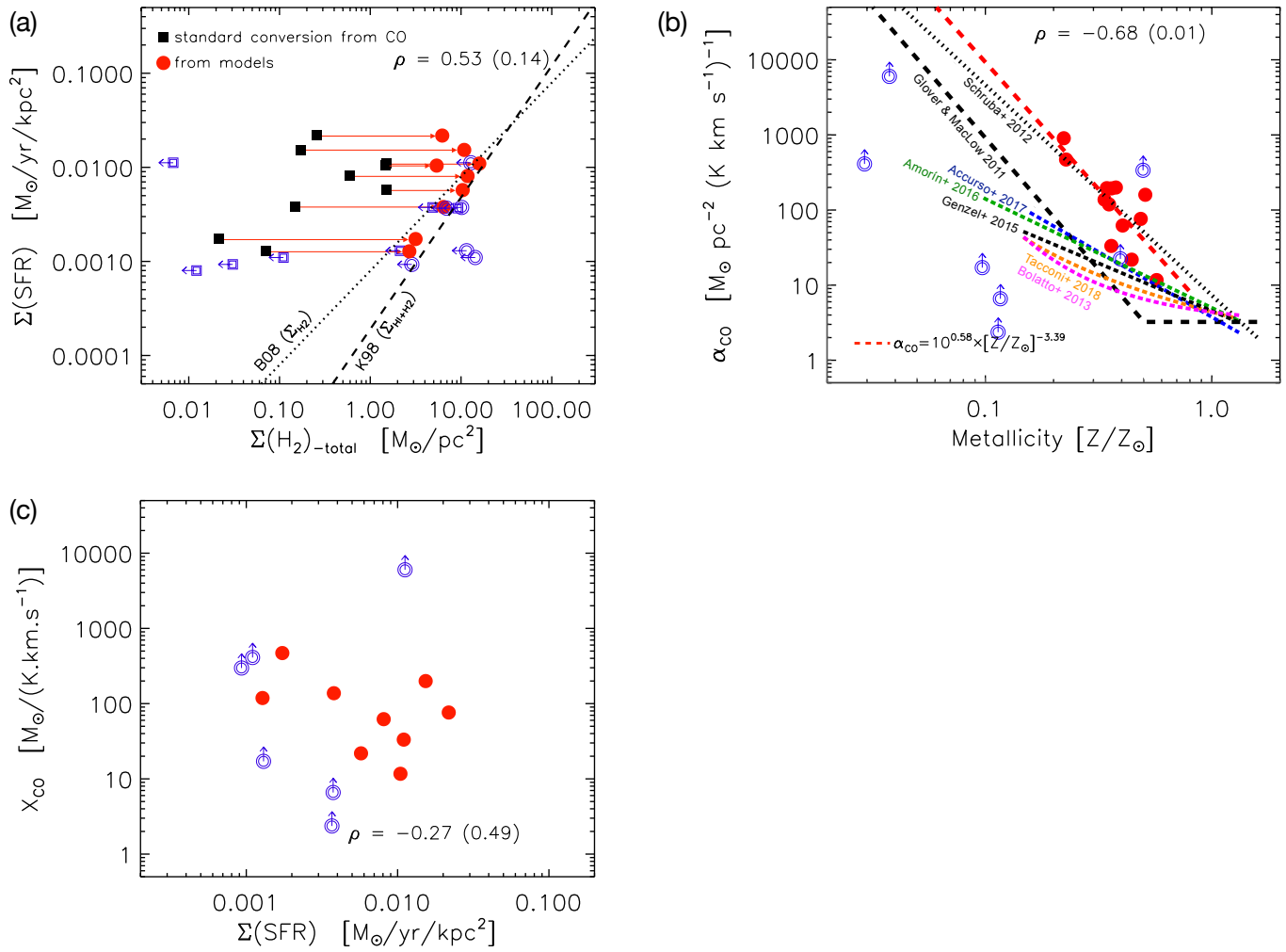

Fig. 10. Consequences of quantifying the total H_2 of the DGS sample. *a*: Schmidt–Kennicutt relationship and Bigiel et al. (2008) revisited. Solid black squares are the values when the M_{H_2} is calculated from the CO-to-H_2 standard conversion factor; solid red dots are the total H_2 determined from our self-consistent models. The dashed line is the usual Schmidt–Kennicutt relation, where low-Z star-forming dwarf galaxies are normally outliers when CO is used to determine the H_2 (Cormier et al. 2014). The dotted line is the Bigiel et al. (2008) relationship determined for the $\Sigma_{SFR}-\Sigma_{gas}$ relationship. *b*: α_{CO} as a function of Z from Schruba et al. (2012; black dotted line), Glover & Mac Low (2011; long black dashed line), Accurso et al. (2017a; blue dashed line), Amorín et al. (2016; green dashed line), Genzel et al. (2015; short black dashed line), Tacconi et al. (2018; orange dashed line), Bolatto et al. (2013; pink dashed line), and our new $\alpha_{CO}-Z$ relationship determined from this paper (red dashed line). Red solid dots are the total H_2 determined from our self-consistent models in this paper. Also given in the panel is the derived expression to determine α_{CO} as a function of Z from this new relationship, which has a standard deviation of 0.32 dex. *c*: X_{CO} conversion factor from this paper and Σ_{SFR}. Spearman correlation coefficients (ρ) and p-values in parenthesis are indicated within each panel. Red dots are DGS galaxies with CO detections. Open symbols in all panels are upper limits due to CO non-detections.

We have determined a $L_{[C\,II]}$-to-M_{H_2} conversion factor: $M(H_2)_{total} = 10^{2.12} \times [L_{[C\,II]}]^{0.97}$ with a standard deviation of 0.14 dex. Following from this, we give a new CO-to-M_{H_2} conversion factor that takes into account the total M_{H_2} –both the CO-dark and CO-bright gas– given by application of the models:

$\alpha_{CO} = 10^{0.58} \times [Z/Z_\odot]^{-3.39}$ with a standard deviation of 0.32 dex.

Comparisons with the fraction of CO-dark gas in the low-metallicity galaxies and their galactic properties reveal the following findings:

1. The fraction of CO-dark gas is correlated with $L_{[C\,II]}/L_{CO(1-0)}$. There is a tight correlation between the [C II]λ158 μm and the total M_{H_2} over the range of low-metallicity galaxies of the DGS.

2. The effective A_V from our models is anticorrelated with $L_{[C\,II]}/L_{CO(1-0)}$ and hence the CO-dark gas fraction. Therefore, the consequence of the effective low A_V overall in low-metallicity galaxies is the extreme $L_{[C\,II]}/L_{CO(1-0)}$ observed in star-forming dwarf galaxies.

3. The SFR, n_H, and G_0 do not individually control the CO-dark gas mass fraction.

4. The CO-dark gas accounts for most (>70%) of the total H_2 over the wide range of galaxy properties of the *Herschel* DGS. This study consists of galaxies with $L_{[C\,II]}/L_{TIR}$ ranging between 0.1 and 0.5%, metallicity values from ~0.02 to 0.6 $Z_\odot$, $L_{[C\,II]}/L_{CO(1-0)}$ values corresponding to two orders of magnitude of M_{H_2} and over three orders of magnitude of L_{FIR} and stellar mass.

5. Our new CO (1−0)-to-M_{H_2} conversion factor as a function of metallicity, which also accounts for the CO-dark M_{H_2}, is

steeper than most others in the literature, but resembles that of Schruba et al. (2012).

6. When taking into account this significant CO-dark H_2 reservoir, the star-forming dwarf galaxies, which were above the Schmidt–Kennicutt relation when only the observed CO (1−0) was used to deduce the H_2 reservoir, now shift to the normal relation of $\Sigma_{SFR}-\Sigma_{M_{H_2}}$ found for star-forming disc galaxies.

7. [C I] shows signs of being a convenient tracer of the M_{H_2}, particularly at low Z where it can be independent of n_H and G_0. However, [C I] is intrinsically less luminous than [C II]. The utility of [C I] as a tracer of total M_{H_2} for a variety of galactic conditions requires further follow-up investigation.

We conclude that the low L_{CO}/SFR and the high $L_{[C\,II]}/L_{CO(1-0)}$ observed in low-metallicity dwarf galaxies can be explained by the photodissociation of CO, and signals the presence of a prominent reservoir of CO-dark H_2. Observations of a larger number of extremely low-Z galaxies is necessary to pin down the lowest Z end of the $\alpha_{CO}-Z$ and the $L_{[C\,II]}-M_{H_2}$ relations as well as to expand the studies of parameter space and spatial scales in galaxies. Likewise, robust comparison of other methods to determine M_{H_2}, and determination of when these different methods are applicable, will be the subject of followup studies.

Acknowledgements. The authors wish to thank the anonymous referee for a number of suggestions that have improved the presentation of this study. We thank A. Poglitsch for valuable discussions that also helped to improve the quality of the paper. We acknowledge support from the DAAD/PROCOPE projects 57210883/35265PE and from the Programme National Physique et Chimie du Milieu Interstellaire (PCMI) of CNRS/INSU with INC/INP co-funded by CEA and CNES. The European Unions Horizon 2020 research and innovation program under the Marie Sklodowska-Curie grant agreement No 702622 supported DC during this study. SH acknowledges financial support from DFG programme HO 5475/2-1. MC acknowledges funding from the Deutsche Forschungsgemeinschaft (DFG, German Research Foundation) through an Emmy Noether Research Group (grant number KR4801/1-1) and the DFG Sachbeihilfe (grant number KR4801/2-1). MG has received funding from the European Research Council (ERC) under the 397 European Union Horizon 2020 research and innovation programme (MagneticYSOs project, grant agreement 398 No 679937). FLP acknowledges funding from the ANR grant LYRICS (ANR-16-CE31-0011). This research was originally made possible through the financial support of the Agence Nationale de la Recherche (ANR) through the programme SYMPATICO (Program Blanc Projet NR-11-BS56-0023) and through the EU FP7. This study made use of *Herschel* observations: PACS was developed by MPE (Germany); UVIE (Austria); KU Leuven, CSL, IMEC (Belgium); CEA, LAM (France); MPIA (Germany); INAFIFSI/OAA/OAP/OAT, LENS, SISSA (Italy); IAC (Spain). This development was supported by BMVIT (Austria), ESA-PRODEX (Belgium), CEA/CNES (France), DLR (Germany), ASI/INAF (Italy), and CICYT/MCYT (Spain). SPIRE was developed by Cardiff University (UK); Univ. Lethbridge (Canada); NAOC (China); CEA, LAM (France); IFSI, Univ. Padua (Italy); IAC (Spain); SNSB (Sweden); Imperial College London, RAL, UCL-MSSL, UKATC, Univ. Sussex (UK) and Caltech, JPL, NHSC, Univ. Colorado (USA). This development was supported by CSA (Canada); NAOC (China); CEA, CNES, CNRS (France); ASI (Italy); MCINN (Spain); Stockholm Observatory (Sweden); STFC (UK); and NASA (USA).

References

Accurso, G., Saintonge, A., Catinella, B., et al. 2017a, MNRAS, 470, 4750
Accurso, G., Saintonge, A., Bisbas, T. G., & Viti, S. 2017b, MNRAS, 464, 3315
Ackermann, M., Ajello, M., Allafort, A., et al. 2012, A&A, 538, A71
Allen, R. J., Hogg, D. E., & Engelke, P. D. 2015, AJ, 149, 123
Amorín, R., Muñoz-Tuñón, C., Aguerri, J. A. L., & Planesas, P. 2016, A&A, 588, A23
Andreani, P., Retana-Montenegro, E., Zhang, Z.-Y., et al. 2018, A&A, 615, A142
Arimoto, N., Sofue, Y., & Tsujimoto, T. 1996, PASJ, 48, 275
Asplund, M., Grevesse, N., Sauval, A. J., & Scott, P. 2009, ARA&A, 47, 481
Bertemes, C., Wuyts, S., Lutz, D., et al. 2018, MNRAS, 478, 1442
Bethermin, M., Fudamoto, Y., Ginolfi, M., et al. 2020, A&A, 643, A2
Bigiel, F., Leroy, A., Walter, F., et al. 2008, AJ, 136, 2846
Bigiel, F., Leroy, A. K., Walter, F., et al. 2011, ApJ, 730, L13
Bisbas, T. G., van Dishoeck, E. F., Papadopoulos, P. P., et al. 2017, ApJ, 839, 90
Bolatto, A. D., Wolfire, M., & Leroy, A. K. 2013, ARA&A, 51, 207
Bothwell, M. S., Aguirre, J. E., Aravena, M., et al. 2017, MNRAS, 466, 2825
Bourne, N., Dunne, L., Bendo, G. J., et al. 2013, MNRAS, 436, 479
Bourne, N., Dunlop, J. S., Simpson, J. M., et al. 2019, MNRAS, 482, 3135
Brauher, J. R., Dale, D. A., & Helou, G. 2008, ApJS, 178, 280
Carilli, C. L., & Walter, F. 2013, ARA&A, 51, 105
Chevance, M., Madden, S. C., Lebouteiller, V., et al. 2016, A&A, 590, A36
Chevance, M., Madden, S. C., Fischer, C., et al. 2020, MNRAS, 494, 5279
Cigan, P., Young, L., Cormier, D., et al. 2016, AJ, 151, 14
Clark, P. C., & Glover, S. C. O. 2015, MNRAS, 452, 2057
Combes, F., García-Burillo, S., Braine, J., et al. 2013, A&A, 550, A41
Cormier, D., Madden, S. C., Hony, S., et al. 2010, A&A, 518, L57
Cormier, D., Lebouteiller, V., Madden, S. C., et al. 2012, A&A, 548, A20
Cormier, D., Madden, S. C., Lebouteiller, V., et al. 2014, A&A, 564, A121
Cormier, D., Madden, S. C., Lebouteiller, V., et al. 2015, A&A, 578, A53
Cormier, D., Bigiel, F., Wang, J., et al. 2016, MNRAS, 463, 1724
Cormier, D., Abel, N. P., Hony, S., et al. 2019, A&A, 626, A23
Croxall, K. V., Smith, J. D., Wolfire, M. G., et al. 2012, ApJ, 747, 81
Croxall, K. V., Smith, J. D., Pellegrini, E., et al. 2017, ApJ, 845, 96
da Cunha, E., Groves, B., Walter, F., et al. 2013, ApJ, 766, 13
Daddi, E., Bournaud, F., Walter, F., et al. 2010, ApJ, 713, 686
Daddi, E., Dannerbauer, H., Liu, D., et al. 2015, A&A, 577, A46
Dale, D. A., Aniano, G., Engelbracht, C. W., et al. 2012, ApJ, 745, 95
de Looze, I., Baes, M., Bendo, G. J., Cortese, L., & Fritz, J. 2011, MNRAS, 416, 2712
De Looze, I., Cormier, D., Lebouteiller, V., et al. 2014, A&A, 568, A62
Dessauges-Zavadsky, M., Ginolfi, M., Pozzi, F., et al. 2020, A&A, 643, A5
Díaz-Santos, T., Armus, L., Charmandaris, V., et al. 2017, ApJ, 846, 32
Eales, S., Smith, M. W. L., Auld, R., et al. 2012, ApJ, 761, 168
Fahrion, K., Cormier, D., Bigiel, F., et al. 2017, A&A, 599, A9
Ferland, G. J., Chatzikos, M., Guzmán, F., et al. 2017, Rev. Mex. Astron. Astrofis., 53, 385
Franeck, A., Walch, S., Seifried, D., et al. 2018, MNRAS, 481, 4277
Galametz, M., Madden, S. C., Galliano, F., et al. 2011, A&A, 532, A56
Gallerani, S., Ferrara, A., Neri, R., & Maiolino, R. 2014, MNRAS, 445, 2848
Galliano, F., Galametz, M., & Jones, A. P. 2018, ARA&A, 56, 673
Genzel, R., Tacconi, L. J., Combes, F., et al. 2012, ApJ, 746, 69
Genzel, R., Tacconi, L. J., Lutz, D., et al. 2015, ApJ, 800, 20
Glover, S. C. O., & Clark, P. C. 2012a, MNRAS, 426, 377
Glover, S. C. O., & Clark, P. C. 2012b, MNRAS, 421, 9
Glover, S. C. O., & Clark, P. C. 2016, MNRAS, 456, 3596
Glover, S. C. O., & Mac Low, M.-M. 2011, MNRAS, 412, 337
Gnedin, N. Y., & Draine, B. T. 2014, ApJ, 795, 37
Gong, M., Ostriker, E. C., & Kim, C.-G. 2018, ApJ, 858, 16
Grenier, I. A., Casandjian, J.-M., & Terrier, R. 2005, Science, 307, 1292
Griffin, M. J., Abergel, A., Abreu, A., et al. 2010, A&A, 518, L3
Grossi, M., Corbelli, E., Bizzocchi, L., et al. 2016, A&A, 590, A27
Groves, B. A., Schinnerer, E., Leroy, A., et al. 2015, ApJ, 799, 96
Gullberg, B., De Breuck, C., Vieira, J. D., et al. 2015, MNRAS, 449, 2883
Habing, H. J. 1968, Bull. Astron. Inst. Neth., 19, 421
Hailey-Dunsheath, S., Nikola, T., Stacey, G. J., et al. 2010, ApJ, 714, L162
Harikane, Y., Ouchi, M., Inoue, A. K., et al. 2020, ApJ, 896, 93
Hashimoto, T., Inoue, A. K., Mawatari, K., et al. 2019, PASJ, 71, 71
Hayashi, K., Mizuno, T., Fukui, Y., et al. 2019, ApJ, 884, 130
Heintz, K. E., & Watson, D. 2020, ApJ, 889, L7
Herrera-Camus, R., Bolatto, A. D., Wolfire, M. G., et al. 2015, ApJ, 800, 1
Herrera-Camus, R., Bolatto, A., Smith, J. D., et al. 2016, ApJ, 826, 175
Hunt, L. K., García-Burillo, S., Casasola, V., et al. 2015, A&A, 583, A114
Hunter, D. A., Kaufman, M., Hollenbach, D. J., et al. 2001, ApJ, 553, 121
Israel, F. P., Maloney, P. R., Geis, N., et al. 1996, ApJ, 465, 738
Jameson, K. E., Bolatto, A. D., Wolfire, M., et al. 2018, ApJ, 853, 111
Jiao, Q., Zhao, Y., Lu, N., et al. 2019, ApJ, 880, 133
Kalberla, P. M. W., Kerp, J., & Haud, U. 2020, A&A, 639, A26
Kamenetzky, J., Rangwala, N., & Glenn, J. 2017, MNRAS, 471, 2917
Kamenetzky, J., Privon, G. C., & Narayanan, D. 2018, ApJ, 859, 9
Kaufman, M. J., Wolfire, M. G., Hollenbach, D. J., & Luhman, M. L. 1999, ApJ, 527, 795
Kaufman, M. J., Wolfire, M. G., & Hollenbach, D. J. 2006, ApJ, 644, 283
Kennicutt, R. C., Jr. 1998, ARA&A, 36, 189
Kennicutt, R. C., Jr., & Evans, N. J. 2012, ARA&A, 50, 531
Kennicutt, R. C., Jr., Calzetti, D., Walter, F., et al. 2007, ApJ, 671, 333
Kewley, L. J., & Ellison, S. L. 2008, ApJ, 681, 1183
Krumholz, M. R., & Gnedin, N. Y. 2011, ApJ, 729, 36
Krumholz, M. R., Leroy, A. K., & McKee, C. F. 2011, ApJ, 731, 25
Kumari, N., Irwin, M. J., & James, B. L. 2020, A&A, 634, A24
Langer, W. D., Velusamy, T., Pineda, J. L., et al. 2010, A&A, 521, L17
Langer, W. D., Velusamy, T., Pineda, J. L., Willacy, K., & Goldsmith, P. F. 2014, A&A, 561, A122
Lapham, R. C., Young, L. M., & Crocker, A. 2017, ApJ, 840, 51

Laporte, N., Katz, H., Ellis, R. S., et al. 2019, MNRAS, 487, L81
Lebouteiller, V., Cormier, D., Madden, S. C., et al. 2012, A&A, 548, A91
Lebouteiller, V., Cormier, D., Madden, S. C., et al. 2019, A&A, 632, A106
Leitherer, C., Ortiz Otálvaro, P. A., Bresolin, F., et al. 2010, ApJS, 189, 309
Leroy, A. K., Walter, F., Brinks, E., et al. 2008, AJ, 136, 2782
Leroy, A. K., Bolatto, A., Bot, C., et al. 2009, ApJ, 702, 352
Leroy, A. K., Bolatto, A., Gordon, K., et al. 2011, ApJ, 737, 12
Leroy, A. K., Bigiel, F., de Blok, W. J. G., et al. 2012, AJ, 144, 3
Leroy, A. K., Walter, F., Sandstrom, K., et al. 2013, AJ, 146, 19
Li, Q., Narayanan, D., Davè, R., & Krumholz, M. R. 2018, ApJ, 869, 73
Liang, L., Feldmann, R., Faucher-Giguère, C.-A., et al. 2018, MNRAS, 478, L83
Liszt, H., Gerin, M., & Grenier, I. 2019, A&A, 627, A95
Lucas, R., & Liszt, H. 1996, A&A, 307, 237
Luhman, M. L., Satyapal, S., Fischer, J., et al. 2003, ApJ, 594, 758
Madden, S. C. 2000, New Astron. Rev., 44, 249
Madden, S. C., & Cormier, D. 2019, in Dwarf Galaxies: From the Deep Universe to the Present, eds. K. B. W. McQuinn, & S. Stierwalt, IAU Symp., 344, 240
Madden, S. C., Poglitsch, A., Geis, N., Stacey, G. J., & Townes, C. H. 1997, ApJ, 483, 200
Madden, S. C., Galametz, M., Cormier, D., et al. 2011, in EAS Publications Series, eds. M. Röllig, R. Simon, V. Ossenkopf, & J. Stutzki, 52, 95
Madden, S. C., Rémy-Ruyer, A., Galametz, M., et al. 2013, PASP, 125, 600
Magdis, G. E., Daddi, E., Elbaz, D., et al. 2011, ApJ, 740, L15
Magnelli, B., Saintonge, A., Lutz, D., et al. 2012, A&A, 548, A22
Malhotra, S., Kaufman, M. J., Hollenbach, D., et al. 2001, ApJ, 561, 766
Maloney, P., & Black, J. H. 1988, ApJ, 325, 389
Murray, C. E., Peek, J. E. G., Lee, M.-Y., & Stanimirović, S. 2018, ApJ, 862, 131
Narayanan, D., Bothwell, M., & Davé, R. 2012, MNRAS, 426, 1178
Nesvadba, N. P. H., Cañameras, R., Kneissl, R., et al. 2019, A&A, 624, A23
Nguyen, H., Dawson, J. R., Miville-Deschênes, M.-A., et al. 2018, ApJ, 862, 49
Nordon, R., & Sternberg, A. 2016, MNRAS, 462, 2804
Offner, S. S. R., Bisbas, T. G., Bell, T. A., & Viti, S. 2014, MNRAS, 440, L81
Papadopoulos, P. P., Thi, W. F., & Viti, S. 2002, ApJ, 579, 270
Papadopoulos, P. P., Thi, W.-F., & Viti, S. 2004, MNRAS, 351, 147
Papadopoulos, P. P., Kovacs, A., Evans, A. S., & Barthel, P. 2008, A&A, 491, 483
Pavesi, R., Sharon, C. E., Riechers, D. A., et al. 2018, ApJ, 864, 49
Pilbratt, G. L., Riedinger, J. R., Passvogel, T., et al. 2010, A&A, 518, L1
Pilyugin, L. S., & Thuan, T. X. 2005, ApJ, 631, 231
Pineda, J. L., Langer, W. D., Velusamy, T., & Goldsmith, P. F. 2013, A&A, 554, A103
Pineda, J. L., Langer, W. D., & Goldsmith, P. F. 2014, A&A, 570, A121
Planck Collaboration XIX. 2011, A&A, 536, A19
Poglitsch, A., Krabbe, A., Madden, S. C., et al. 1995, ApJ, 454, 293
Poglitsch, A., Waelkens, C., Geis, N., et al. 2010, A&A, 518, L2
Polles, F. L., Madden, S. C., Lebouteiller, V., et al. 2019, A&A, 622, A119
Popping, G., Decarli, R., Man, A. W. S., et al. 2017, A&A, 602, A11
Privon, G. C., Narayanan, D., & Davé, R. 2018, ApJ, 867, 102
Reach, W. T., Heiles, C., & Bernard, J.-P. 2015, ApJ, 811, 118
Reach, W. T., Heiles, C., & Bernard, J.-P. 2017, ApJ, 834, 63
Rémy-Ruyer, A., Madden, S. C., Galliano, F., et al. 2013, A&A, 557, A95
Rémy-Ruyer, A., Madden, S. C., Galliano, F., et al. 2014, A&A, 563, A31
Rémy-Ruyer, A., Madden, S. C., Galliano, F., et al. 2015, A&A, 582, A121
Requena-Torres, M. A., Israel, F. P., Okada, Y., et al. 2016, A&A, 589, A28
Röllig, M., Ossenkopf, V., Jeyakumar, S., Stutzki, J., & Sternberg, A. 2006, A&A, 451, 917
Roman-Duval, J., Gordon, K. D., Meixner, M., et al. 2014, ApJ, 797, 86
Roussel, H., Helou, G., Hollenbach, D. J., et al. 2007, ApJ, 669, 959
Roychowdhury, S., Chengalur, J. N., Begum, A., & Karachentsev, I. D. 2009, MNRAS, 397, 1435
Saintonge, A., Catinella, B., Tacconi, L. J., et al. 2017, ApJS, 233, 22
Sandstrom, K. M., Leroy, A. K., Walter, F., et al. 2013, ApJ, 777, 5
Schaerer, D., Ginolfi, M., Bethermin, M., et al. 2020, A&A, 643, A3
Schruba, A., Leroy, A. K., Walter, F., et al. 2012, AJ, 143, 138
Scoville, N., Sheth, K., Aussel, H., et al. 2016, ApJ, 820, 83
Seifried, D., Haid, S., Walch, S., Borchert, E. M. A., & Bisbas, T. G. 2020, MNRAS, 492, 1465
Shetty, R., Glover, S. C., Dullemond, C. P., & Klessen, R. S. 2011, MNRAS, 412, 1686
Smith, B. J., & Madden, S. C. 1997, AJ, 114, 138
Smith, R. J., Glover, S. C. O., Clark, P. C., Klessen, R. S., & Springel, V. 2014, MNRAS, 441, 1628
Smith, J. D. T., Croxall, K., Draine, B., et al. 2017, ApJ, 834, 5
Stacey, G. J., Geis, N., Genzel, R., et al. 1991, ApJ, 373, 423
Stacey, G. J., Hailey-Dunsheath, S., Ferkinhoff, C., et al. 2010, ApJ, 724, 957
Sutter, J., Dale, D. A., Croxall, K. V., et al. 2019, ApJ, 886, 60
Tacconi, L. J., Genzel, R., Neri, R., et al. 2010, Nature, 463, 781
Tacconi, L. J., Genzel, R., Saintonge, A., et al. 2018, ApJ, 853, 179
Tacconi, L. J., Genzel, R., & Sternberg, A. 2020, ARA&A, 58, 157
Tamura, Y., Mawatari, K., Hashimoto, T., et al. 2019, ApJ, 874, 27
Tang, N., Li, D., Heiles, C., et al. 2016, A&A, 593, A42
Togi, A., & Smith, J. D. T. 2016, ApJ, 830, 18
Tomassetti, M., Porciani, C., Romano-Diaz, E., Ludlow, A. D., & Papadopoulos, P. P. 2014, MNRAS, 445, L124
Valentino, F., Magdis, G. E., Daddi, E., et al. 2020, ApJ, 890, 24
Vallini, L., Pallottini, A., Ferrara, A., et al. 2018, MNRAS, 473, 271
van der Laan, T. P. R., Armus, L., Beirao, P., et al. 2015, A&A, 575, A83
Walter, F., Decarli, R., Sargent, M., et al. 2014, ApJ, 782, 79
Wolfire, M. G., Hollenbach, D., & McKee, C. F. 2010, ApJ, 716, 1191
Xu, D., Li, D., Yue, N., & Goldsmith, P. F. 2016, ApJ, 819, 22
Zanella, A., Daddi, E., Magdis, G., et al. 2018, MNRAS, 481, 1976

Appendix A: Cloudy model details

For this study we use Cloudy models similar to those originating from Cormier et al. (2019, 2015) for which we have adopted a closed spherical geometry with an internal and isotropic ionising source surrounded by a 4π steradian layer of H II region, and a neutral PDR layer surrounding the ionised layer. The source ionises the inner edge of the cloud and the radiation is propagated through the H II region self-consistently making the transition into the PDR. The evolution of mass components is calculated based on integrating the density over the volume of the spherical shell at each depth into the cloud.

The model central source is a continuous starburst of 7 Myr from Starburst99 (Leitherer et al. 2010) for a total source luminosity of $10^9\,L_\odot$. Cloudy allows the choice of calculations in luminosity or in intensity. We selected the luminosity case for the SED brightness, where the photon luminosity of the central source impacts the cloud beginning at the inner edge of the ionised region (at the start of the H II region), $r_{\rm in}$, which, for these models is varied from $\log(r_{\rm in}\,{\rm cm}) = 20.0$ to 21.3, in steps of 0.3 dex. The initial hydrogen density ($n_{\rm H}$) at the illuminated edge of the cloud is varied from 10 to $10^4\,{\rm cm}^{-3}$. While the initial ionisation parameter, U, can be an input command only in the intensity case, for our luminosity case, we chose to effectively have a range of U in the luminosity case, by varying $r_{\rm in}$ as an input parameter, which in turn varies U, which is deduced within Cloudy for each model:

$$U = \frac{Q(H)}{4\pi r_{\rm in}^2 n_{\rm H} c}, \tag{A.1}$$

where $Q(H)$ is the number of hydrogen-ionising photons emitted by the central source, and c is the speed of light. The intensity of the FUV radiation at the PDR front, G_0, deduced in our Cloudy models, ranges from ∼17 to 11 481 in units of the Habing radiation field ($1.6\times10^{-3}\,{\rm ergs\,cm^{-2}\,s^{-1}}$; Habing 1968). Five metallicity bins were calculated for the models: Z = 0.05, 0.1, 0.25, 0.5, and $1.0\,Z_\odot$.

The dust and PAH properties used in this model are described in Cormier et al. (2019). The opacity curves of the SMC are used. The abundance of PAHs is further reduced by metallicity to the power of 1.3, characterising the prominent drop in PAH abundance at lower metallicity (e.g. Rémy-Ruyer et al. 2014, 2015). Tests performed in Cormier et al. (2019), inspecting the sensitivity of the PAH abundance, concluded that the PAH abundance is not an important factor in the outcome of the model results because the grain abundance is always larger than the already-reduced PAH abundance.

In Cloudy it is possible to choose a constant density throughout the cloud or to assume that the total pressure is constant. Cormier et al. (2019) looked into different approaches of the density law for a constant pressure case versus a constant density case and have found a compromise of these two extreme cases that works best in predicting the observations for the DGS sources. An intermediate case for the assumed density profile is constructed which is constant in the H II region and increases linearly with the hydrogen column density in the neutral gas. The different cases of constant density, constant pressure and smoothly-increasing density law were tested in Cormier et al. (2019) where, for example, the constant density models predict less [O I] emission and the constant pressure models predict more [O I] emission than the smoothly increasing density law adopted, which was found to successfully describe the observations.

A full galaxy has numerous stellar clusters and H II regions and ensembles of PDR/molecular clouds. To go from a model single cluster-plus-cloud system to a representation of a full galaxy with numerous cluster-plus-cloud systems, we create a "unit model" with total source luminosity = $10^9\,L_\odot$. The unit model of $10^9\,L_\odot$ chosen here is arbitrary but serves as a representative order of magnitude of luminosity of the observed galaxies. Thus all of the line luminosities predicted by the model correspond to a model for which $L = 10^9\,L_\odot$. The output masses are also determined for a model with source $L = 10^9\,L_\odot$. Since mass scales with luminosity, the masses determined for an individual galaxy, having $L_{\rm TIR}$ (galaxy), are scaled by $L_{\rm TIR}$ (galaxy)/$10^9\,L_\odot$. This approximation assumes an energy balance between UV-optical and IR and that $L_{\rm TIR}$ scales similarly to the luminosity in the hydrogen-ionising energy range (Cormier et al. 2012). We refer to Cormier et al. (2019) for further details and input parameter studies of a similar model used for this study.